3-2020

Neutron Displacement Damage in Germanium Tin Photodiodes

Nathan J. Gale

Neutron Displacement Damage in Germanium-Tin Photodiodes

THESIS

Nathan J. Gale, 2d Lt, USAF

AFIT-ENP-MS-20-M-096

DEPARTMENT OF THE AIR FORCE
AIR UNIVERSITY

AIR FORCE INSTITUTE OF TECHNOLOGY

Wright-Patterson Air Force Base, Ohio

AFIT-ENP-MS-20-M-096

NEUTRON DISPLACEMENT DAMAGE IN GERMANIUM-TIN PHOTODIODES

THESIS

Presented to the Faculty

Department of Engineering Physics

Graduate School of Engineering and Management

Air Force Institute of Technology

Air University

Air Education and Training Command

in Partial Fulfillment of the Requirements for the

Degree of Master of Science

Nathan J. Gale, BS

2d Lt, USAF

March 2020

AFIT-ENP-MS-20-M-096

NEUTRON DISPLACEMENT DAMAGE IN GERMANIUM-TIN PHOTODIODES

THESIS

Nathan J. Gale, BS
2d Lt, USAF

Committee Membership:

John W. McClory, PhD
Chair

E. Lee Hobbs, PhD
Member

Michael R. Hogsed, PhD
Member

Abstract

GeSn is a promising material for photodiodes in the near-to-mid infrared (IR) spectrum because of new growth methods that enable integration with complementary metal oxide semiconductor (CMOS) technology. While natural germanium has a threshold wavelength of 1800 nm, 6.9% Sn content extends the threshold wavelength to 2700 nm based on a Sn content dependent bandgap. Also, unlike other semiconductors that require liquid nitrogen cooling to act as an IR sensor, GeSn can be operated at room temperature, enabling a wide variety of applications. In this study, photodiodes ranging from 0% to 6.9% tin content were subjected to 1 MeV (Si) equivalent neutron radiation ranging from $4 \times 10^{12}\,\mathrm{cm}^{-2}$ to $4 \times 10^{14}\,\mathrm{cm}^{-2}$. IV curves, CV curves, and relative photoresponse were measured before and after irradiation to observe change due to displacement damage. While the change in IV measurements varied widely, the photoresponse more than doubled for all irradiated samples, contrary to expectation. The samples of low tin content had a greater increase (as much as 1100%) than high tin content samples (ranging from 100% to 400%). Deep-level transient Fourier spectroscopy (DLTFS) was also used to measure defect levels. The 0% and 6.8% tin samples showed defects at energies of 0.26 eV below the conduction band and 0.17 eV above the valence band, respectively. The 0.26 eV trap is attributed to an A center vacancy-oxygen (V-O) complex and the 0.17 eV trap is attributed to a vacancy-phosphorous (V-P) defect.

Acknowledgements

Abrazos, no balazos. -Andres Manuel Lopez Obrador

I am profoundly grateful to everyone who has contributed to my education – graduate and otherwise – that has helped prepare me for my mission as an Air Force nuclear engineer. No one gets anywhere in life (or the Air Force) without a large helping of advice, assistance, and mercy from the surrounding community, so I would like to take this opportunity to thank the following people and organizations:

- The Air Force Office of Scientific Research for funding this research, without which I would have no experiment to conduct or analyze.
- My committee members for all their advice in writing this thesis and patience to explain even the most trivial concepts to me.
- Dr. Buguo Wang for his invaluable support in planning and conducting the photodiode characterization measurements, particularly the DLTFS and CV measurements taken in his lab at Wright State University.
- All of the professors and post-doctoral fellows in the AFIT nuclear engineering program for providing a truly unique and first-class educational experience.
- Dr. John Kouvetakis of Arizona State University for providing the photodiodes used in this study.
- The Ohio State University Nuclear Reactor Laboratory for providing an excellent resource for radiation damage studies and for helping me account for many important details in this study.

- Dr. Adam Hecht, Dr. Cassiano de Oliveira, Colonel Fred Garcia, and Lieutenant Colonel Neal Kleinschmidt for mentoring me in defense-related nuclear engineering at the University of New Mexico and encouraging me to apply to the AFIT graduate program.

- Commander Jamie Doule, Lieutenant Commander Stephen White, Chief Petty Officer Oscar Magallanes, and Chief Petty Officer Bill Gale for mentoring and encouraging me to serve in the U.S. military, even if they would have preferred that I serve in the Navy.

- My father for encouraging me to be an engineer long before I even knew what engineering was; and my mother for providing my education through the eighth grade and supporting me in countless extracurricular activities.

- My brothers and sisters for their unfailing love and friendship.

- My beloved and beautiful wife for countless and infinite reasons that I could never thank her enough for, but mostly for having the patience and faith to accompany me and form a family together while I work to accomplish my mission as an Air Force officer. Te quiero güerita.

Nathan J. Gale

Table of Contents

List of Figures

Figure Page

List of Tables

NEUTRON DISPLACEMENT DAMAGE IN GERMANIUM-TIN PHOTODIODES

I. Introduction

Photonics is the field of physics that deals with the generation and detection of light particles. By manipulating the emission, detection, and transmission of photons, they may be used for a variety of applications including lasers, medical instruments, consumer electronics, and fiber optic telecommunications. Infrared radiation detection is especially important for defense applications that include plume chemical spectral analysis, night vision [1], and muzzle detection, potentially in full daylight [12]. In space, photodiodes are used as detectors while light emitting diodes are used to provide isolation between electrical signals [13]. One of the most ambitious applications of these devices is in the Space Based Infrared System which has the missions of missile warning, missile defense, technical intelligence, and battlespace characterization [14].

Due to silicon's dominant position in the semiconductor industry, it is the material of choice for many photonics applications. However, silicon has a band gap of 1.12 eV which corresponds to a threshold wavelength of 1107 nm in the near infrared (NIR) part of the electromagnetic spectrum. To conduct photonics in longer wavelengths of the infrared, a semiconductor with a smaller band gap must be used. As shown in Figure 1, several materials fulfill this requirement and have been used in the past including InGaAs, InAs, InSb, and HgCdTe. The drawback with these materials is that they generally require liquid nitrogen cooling for operation [1]. These materials use group III-V elements, so they are also difficult to integrate with silicon based materials because they may act as dopants for group IV materials. Assuring that

the group III-V materials do not unintentionally increase carrier concentrations in adjacent silicon components adds complexity and cost to production [15].

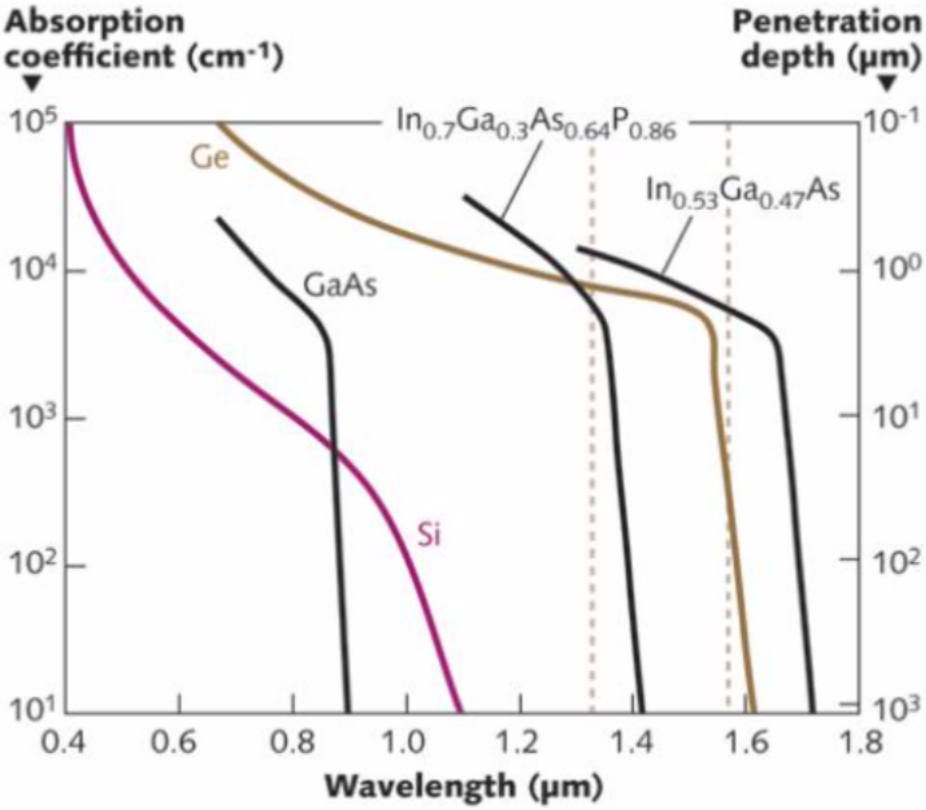

Figure 1. Absorption coefficient of common semiconductor materials as a function of light wavelength. Reproduced with permission from [1].

Germanium is a group IV semiconductor that avoids these cost and operational challenges. Although there is a 4.2% lattice mismatch between germanium and silicon [16], several growth methods have been developed that use SiGe buffer layers and allow integration of germanium on a silicon substrate with good results [1]. The germanium band gap is 0.66 eV, but by alloying with tin, the band gap can be reduced. Dependent on tin percentage, the threshold wavelength can be extended beyond 1800 nm; in this study, the samples of highest tin content, 6.9%, had a threshold wavelength of approximately 2700 nm. Photodiodes of a variety of tin percentages were grown at

Arizona State University (ASU) successfully showing good rectifying behavior [17], and were used in this investigation.

As with any other material in development, the characterization of the radiation hardness of GeSn is important for planning its use, especially for potential defense and space applications. An investigation of proton damage has been performed, however in some samples there was an improvement in electroluminescence post-irradiation, contrary to expectation [11]. Due to their charge, protons cause total ionizing dose (TID) and displacement damage effects. Neutron irradiation was used in this study to limit the effects of TID and compare the defect production in the experiments with the goal of increasing the confidence of post-irradiation effect attribution to displacement damage. Additionally, it is useful to study neutron damage in GeSn to be able to predict the survivability of this material if near a nuclear detonation.

1.1 Research Objectives

The main purpose of this study was to continue characterization of the radiation sensitivity of $Ge_{1-x}Sn_x$ photodiodes to provide information about the advantage and disadvantages of increasing the tin content in these semiconductors. Deep-level transient Fourier spectroscopy (DLTFS) was used to quantify defect formation in the irradiated devices and attribute those defects to specific complexes by comparing their energy level to past studies. Another major motivation was to observe if there would be any improvement in diode performance as was measured in the electroluminescence of some of the samples studied by Choe [11].

1.2 Experiment and Expectations

Five different types of germanium and GeSn photodiodes were provided by ASU with tin contents ranging from 0% to 6.9%. These were cut to provide four samples

of each tin content level and grouped so a sample of each photodiode type could be irradiated at a different neutron fluence level. The Ohio State University (OSU) nuclear reactor was the source of 1 MeV (Si) equivalent neutrons and the samples were irradiated at fluences of 0, 4×10^{12}, 4×10^{13}, and 4×10^{14} cm^{-2}. The purpose of this experimental design was an attempt to correlate radiation damage and device performance with neutron fluence and tin content. To assess device performance, current-voltage (IV) curves were collected for each sample before and after irradiation and the responsivity of each sample was characterized by measuring the photocurrent through the diode at varying light intensities. To measure the defects caused by displacement damage, DLTFS analysis was performed on each sample. Part of the DLTFS process also involved measuring the capacitance-voltage (CV) curve of the samples at various temperatures. The CV data was later used to calculate the carrier depth profile of the samples.

Past studies have shown an increase in dark current [18] and a relaxation of the rectifying behavior of the photodiode in which the reverse bias current increases and the forward bias current decreases post-irradiation [2]. While the correlation is not perfect, past studies of the diodes used in this investigation have shown that the rectifying behavior generally worsens with increasing tin content [17] [19], and that samples of low tin content had a higher degree of change in rectifying behavior post irradiation than high tin content samples (although the absolute increase in reverse bias dark current was greatest in the high tin content samples) [11].

The responsivity of photodiodes has been shown to degrade with increasing radiation flux in many past studies [20] [21] [22] [23] [24]. However, in some materials neutron damage has initially caused an improvement in photoresponse before causing degradation at higher fluence levels [25] [26]. Below the threshold wavelength, the photoresponse has also been shown to have a small improvement with increasing tin

content, but this improvement becomes negligible for wavelengths below about 1300 nm [17].

DLTS measurements have been made of GeSn samples after proton irradiation resulting in the identification of several majority carrier traps and their energy levels within the band gap [27] [28]. These traps have been attributed to divacancy [29], tin-vacancy [30] [31], and phosphorous-vacancy defect complexes [32]. It is expected that these defects will also be produced from neutron damage, but with lower concentration because the non-ionizing energy loss (NIEL) which causes displacement damage defects is higher for protons than for neutrons of the same energy [5].

1.3 Thesis Organization

The first part of chapter 2 explores band gap theory, photodiode modeling, and expected behavior for IV and photoresponse measurements. The different types of displacement damage are explained with emphasis on defects that cause deep-level traps that serve as recombination-generation centers. Finally, the theory of capacitance transience measurements and the DLTFS method is explained with comparison to the conventional DLTS method.

Chapter 3 details the equipment and procedures that were used to perform IV, photoresponse, and DLTFS measurements. Details about the parameters of the photodiodes used are provided along with a short explanation of the fabrication process used at ASU. The irradiation process performed at the OSU reactor is also explained.

Chapter 4 summarizes the results of the measurements and in chapter 5 conclusions are drawn about the results. Some comparison is made to past experiments and explanations of deviations from expectations are given. Finally, ideas for future work are suggested.

II. Background and Theory

2.1 Photodiodes

Photodiodes are designed to convert light into an electrical current, so they are useful as detectors. Any p-n junction can function as a photodiode, but p-i-n junctions are a significant improvement because the intrinsic semiconductor serves to increase the size of the depletion region in which photons are detected. This increased detection volume increases the efficiency of the detector [33]. Figure 2 shows a simplified schematic and energy band diagram of a p-i-n junction. The energy band diagram is generally non-linear near the layer boundaries causing small obstacles to charge flow [34], but these obstacles are overcome by the electric field, so this non-linearity is considered negligible for the purposes of this study.

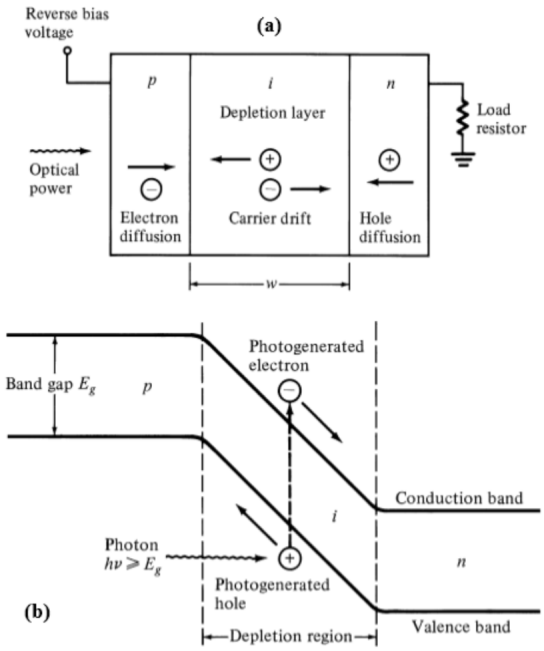

Figure 2. (a) Schematic of a p-i-n junction and (b) the energy band diagram of the same junction. Reproduced with permission from [1].

Applying a reverse bias to the p-i-n junction causes holes to build up in the n

layer and electrons in the p layer, further increasing the electric field and widening the depletion region. This has the effect of reducing the likelihood of thermal diffusion of charge across the p-i-n junction, so dark current is suppressed. Applying a forward bias has the opposite effect, reducing the depletion region width and causing free flow of electrons and holes. This characteristic is referred to as rectifying behavior and an example is displayed in Figure 3.a. After irradiation, displacement damage causes greater dark current in reverse bias and a decrease in forward bias dark current at moderate bias. This is referred to as relaxation of the rectifying behavior and displayed in Figure 3.b.

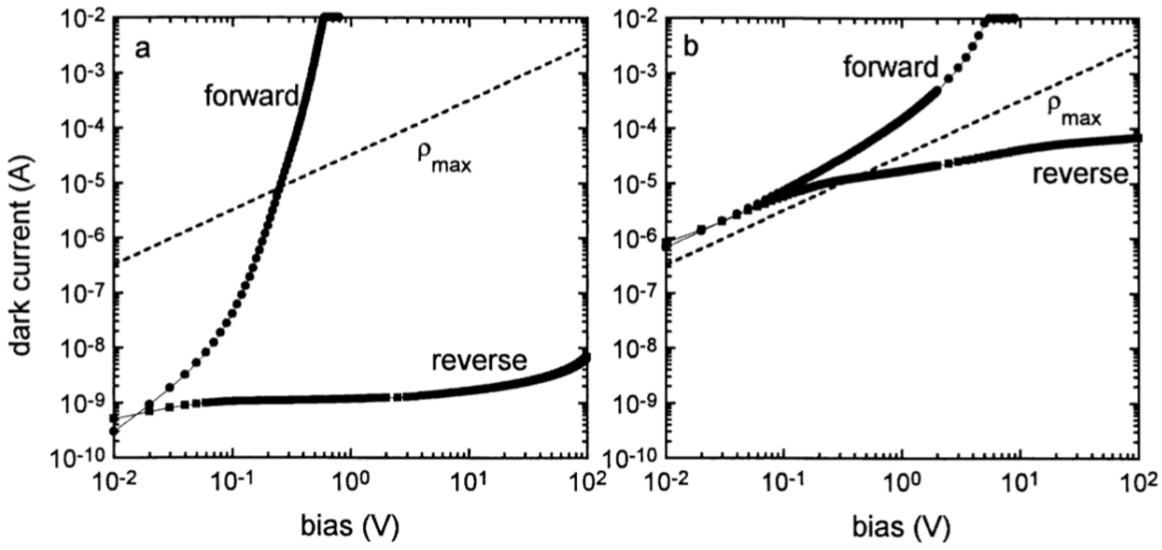

Figure 3. (a) Rectifying behavior of a silicon photodiode and (b) relaxation of rectifying behavior post $2.5 \times 10^{14}\,\mathrm{cm}^{-2}$ fluence of 1 MeV neutrons. Reproduced with permission from [2].

One of the main interests in GeSn as a semiconductor material stems from its tuneable band gap which is achieved by strain engineering. Figure 4 shows that in silicon, the band gap decreases with either tensile strain or compressive strain.

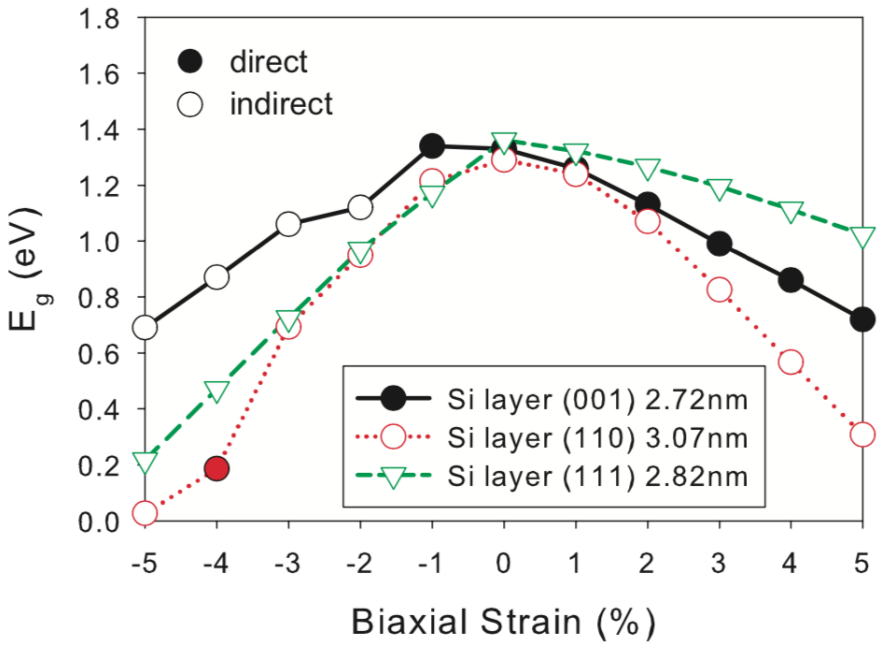

Figure 4. Band gap of three surface orientations of silicon varying with strain. Compressive strain is negative and tensile strain is positive. Reproduced with permission from [3].

Figure 4 also shows that the the band gap energy differs dependent on the band gap type, either direct or indirect. This concept is explained by modelling the electrons' periodic potential, ϕ_k, by a Bloch function as shown in Equation 1.

$$\phi_k(x) = u_k(x)e^{(ikx)} \tag{1}$$

In Equation 1, $u_k(x)$ is a periodic function, x is one-dimensional space along an axis of symmetry in the crystal structure, and k is the indexing vector of the plane wave described by the function [35]. Then the energy band structure can be modelled by plotting the electron energy in the valence and conduction bands against the plane wave vectors, k. These plots become quite complex, but can be simplified for our purposes by plotting only in the first Brillouin zone, the unit cell that most simply defines the reciprocal lattice [35].

Figure 5.a shows a direct band gap structure in which the smallest energy difference between the valence and conduction bands happens to be where the electrons share the same wave vector. However, for the indirect band gap structure shown in Figure 5.b, the smallest energy difference between bands is not aligned along the same wave vector. In order to get across this energy gap, the electrons in the valence band must first be assisted by the thermal energy associated with lattice vibration quanta, called phonons [33]. This excitation changes the wave function of the electrons and if it matches the wave function of the indirect band gap valley, the transition can be achieved.

Figure 5.c shows how the electron energy of the conduction band decreases with increasing tin content. Although germanium is naturally an indirect semiconductor, when alloyed with enough tin it eventually becomes a direct semiconductor, implying an increase in the materials photoresponse efficiency. Previous studies have found that this change occurs at approximately 9% tin content [17].

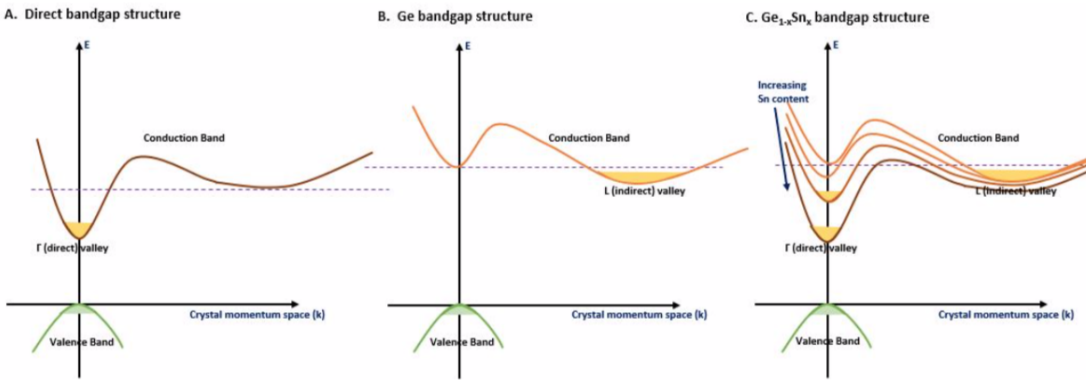

Figure 5. Electron energy versus plane wave vectors, k, in first Brillouin zone for (a) a direct band gap semiconductor, (b) germanium, an indirect semiconductor, and (c) GeSn which transitions from an indirect to a direct band structure as tin content increases. Reproduced with permission from [4].

The properties of the intrinsic region of the photodiode types used in this study are summarized in Table 1 because the intrinsic region is of the greatest importance for the detection properties of the diodes (schematics of the diode types are included

in the appendix). Note that although none of the photodiodes of this study have high enough tin content to transition to direct semiconductors, the indirect band gap is still lowered as shown in Figure 5. Also, for the materials with higher tin content (near 7% in this study), the direct band gap is only marginally greater than the indirect band gap, so the increase in efficiency applies to all but the photons that have energy between the direct and indirect threshold energies.

Table 1. Properties of photodiodes used in this study. Conditions given for room temperature and zero bias.

Diode Type Name	i-% Sn	i-Thickness (nm)	i-Strain (%)	Indirect band gap (eV)[36]	Direct band gap (eV) [36]
Ge472	0	790	0.11	0.66	0.80
GeSnGePiN13	2	530	-0.04	0.62	0.72
GeSnGePiN9A	5.3	440	-0.16	0.57	0.61
GeSnGePiN60A	6.8	675	-0.21	0.54	0.56
GeSnGePiN12	6.9	400	-0.22	0.54	0.55

2.2 Displacement Damage and Defects

A defect is any irregularity in a crystal lattice such as a stacking fault, edge dislocation, a lattice vacancy, an interstitial atom, or substitution with a foreign atom. These are often produced due to imperfections in the crystal growth process, but they can also be intentional as is the case for dopant atoms. Defects caused by irradiation damage consist of a particle knocking an atom out of its lattice position, causing a vacancy and an interstitial to be produced as shown in Figure 6. If the resultant interstitial and vacancy are placed close to each other, they form an unstable defect called a Frenkel pair which usually is produced by particles depositing less than

100 eV of non-ionizing energy [7] and anneals within a millisecond of formation [5].

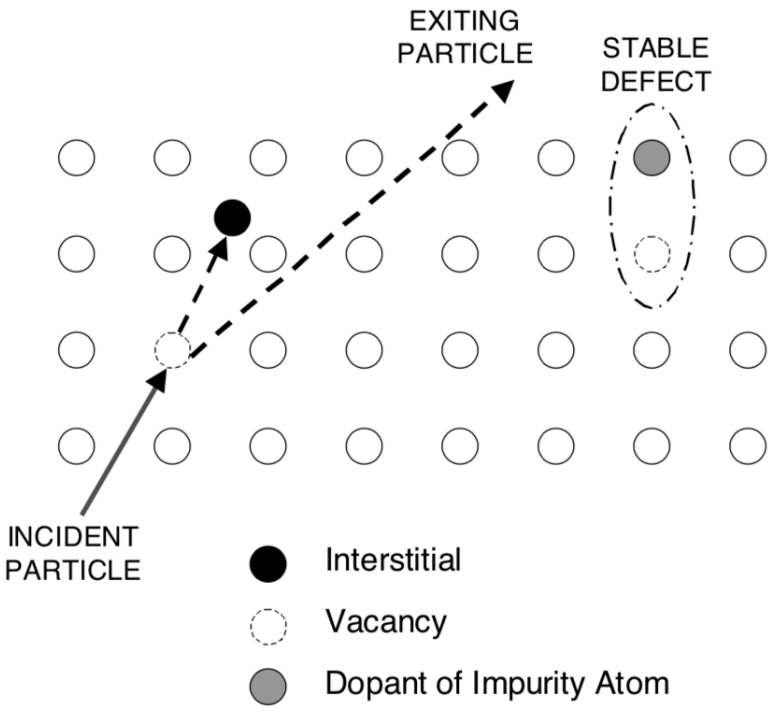

Figure 6. Production of Frenkel pairs and stable defects in a crystal lattice due to radiation interaction. Reproduced with permission from [5].

Defects have a greater effect on the crystal lattice when the interstitial is knocked far enough away to allow the vacancy to survive a much longer period of time. The vacancy may remain isolated, join together with another to form a divacancy, or migrate until it interacts with a dopant or impurity atom. In many cases, the defect becomes electrically active and, if its concentration is high enough, it affects the band gap structure of the semiconductor [5]. For example, Figure 7 shows an example of an electron trap or net acceptor defect in a silicon lattice. The oxygen impurity bonds with the neighboring silicon atoms and the neighboring vacancy. The two silicon atoms separated by the vacancy come together to form a covalent bond, but there is then an additional electron provided by the oxygen atom trapped in the bond [6]. An analogous defect has also been observed in germanium [37]. Similar interactions occur in germanium with dopants like phosphorous and antimony to form stable defects [38],

and in GeSn, the tin atoms may also form defect complexes with vacancies [30]. These defects create energy levels within the band gap whose position is distinctive of the defect type and used for identification.

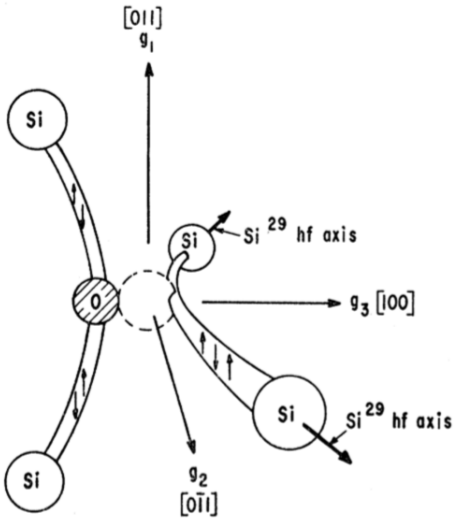

Figure 7. Stable defect in silicon lattice in which an oxygen atom bonds with neighboring silicon atoms and interacts with the neighboring vacancy. Reproduced with permission from [6].

If a defect energy level is close to the valence or conduction band, it will simply capture a carrier that will subsequently return to the band it came from. However, if the defect energy level is near the middle of the band gap, it is considered a deep-level impurity and will act as a recombination-generation center. Mathematically, it is convenient to consider four mechanisms that may take place in these centers: electron capture, electron emission, hole capture, and hole emission as described by the Shockley-Read-Hall model [33]. However, the process can be more simply understood qualitatively as an electron excited from the valence band to the conduction band, assisted by the intermediate trap level that allows it to take smaller energy "steps" [39]. The closer the defect energy level is to the middle of the band gap, the more effective it is at assisting electron excitation or in mathematical terms, the recombination-generation rate increases as defect energy approaches the middle of

the band gap [7].

In p-i-n junctions, the effect of defects is magnified because of the electric field in the depletion region. Figure 8 shows how a defect affects the electronic band structure in and outside of the depletion region. The electric field lowers the barrier to electron emission from the trap to the conduction band and the barrier to hole emission from the trap to the valence band [7]. This phenomenon, called the Poole-Frenkel effect, results in a lower thermal energy requirement for carrier emission and also facilitates phonon-assisted tunneling through the energy barrier [40]. These effects ultimately combine to cause an increase in dark current.

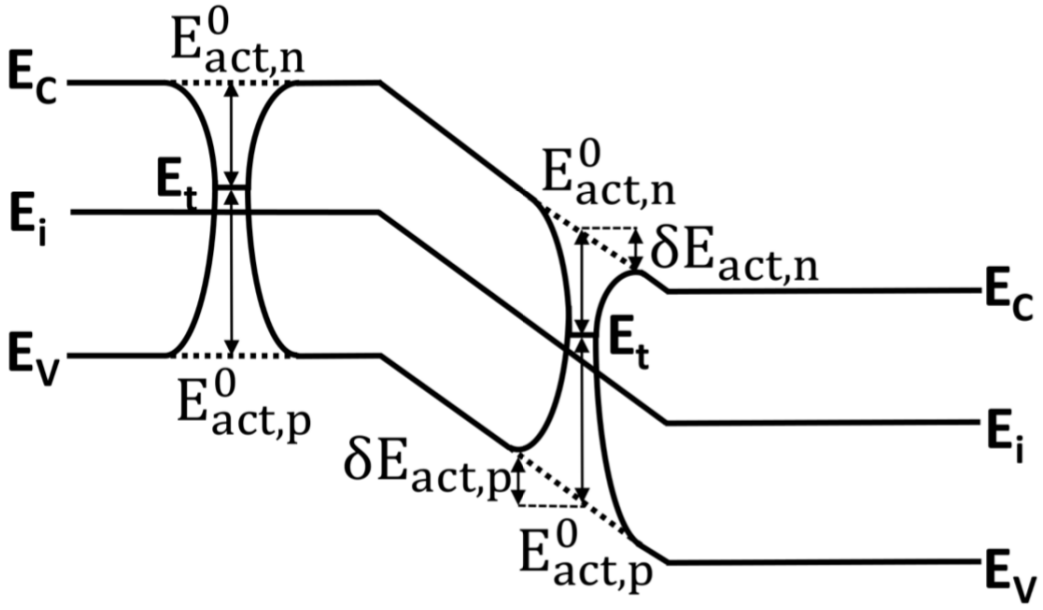

Figure 8. Effect of deep-level traps on the electronic band structure with and without electric field. Reproduced with permission from [7].

Defects may be measured by direct probing methods like deep-level transient spectroscopy (DLTS, described below) or indirectly by attempting to correlate the displacement damage with some change in device performance, such as responsivity, R.

The change in performance is assumed to be proportional to the radiation fluence, Φ,

$$\Delta R(E) = K(E) * \Phi(E), \tag{2}$$

where K is called the displacement damage factor [5]. It in turn is proportional to the non-ionizing energy loss ($NIEL$) by some factor C:

$$K(E) = C * NIEL(E). \tag{3}$$

As the name suggests, the $NIEL$ concept attempts to predict the amount of energy loss of the incident particle that goes into displacement of the crystal lattice atoms, not energy lost to ionization of electrons. Its value is dependent on energy and particle type as shown in Figure 9. Note that for neutrons, $NIEL$ is only given at one energy. This is because uncharged particles like neutrons undergo energy loss interactions that are statistical and much less predictable than charge particle energy loss, so it is more difficult to determine a $NIEL$ value for them [41]. 1 MeV equivalent neutrons are the standard reference point for neutrons displacement damage effects, so its value is provided in Figure 9.

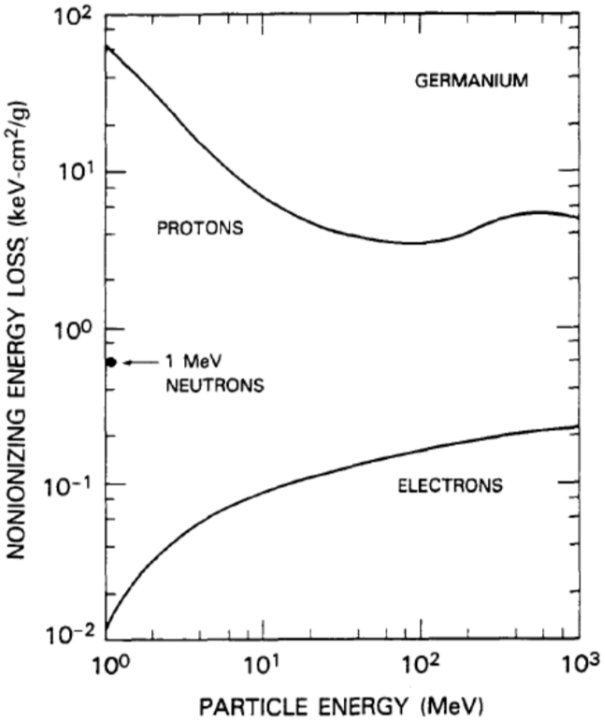

Figure 9. NIEL as a function of energy for radiation particles incident on germanium. Note that for neutrons, the only given value is for a neutron energy of 1 MeV. Reproduced with permission from [8].

2.3 Photoresponse

While photoresponse refers to any measurable response to light, in the context of photodiodes the measurement of interest is the electrical output due to light exposure. The responsivity, R, can be expressed by:

$$R = \eta \frac{q}{hf}, \tag{4}$$

where η is the efficiency of photoelectron creation due to incident light (often called the quantum efficiency), q is the fundamental charge of an electron, h is Planck's constant, and f is the frequency of the signal [42]. For this study, only one optical frequency was used, so the responsivity measurement effectively acts as a measure of

the photodiode's quantum efficiency.

Hamady has used numerical methods to simulate the effect of doping and traps on the quantum efficiency of AlGaN ultraviolet detectors. Using the Athena code to simulate device processing and the 2D device simulator code, Atlas, to solve Poisson's equation, the device transport properties were analyzed using the diffusion-drift model of electron and hole current. Although the model was made specifically for one type of detector, Poisson's equation is fundamental to model semiconductors p-n and p-i-n junctions [33], and the diffusion-drift model is widely used to approximate charge transport in semiconductors [43], so conceptually the results are applicable to other detectors such as the GeSn photodiodes used in this study. Figure 10 shows that there is an optimum dopant level to maximize the quantum efficiency of the detector. Figure 11 shows an increase in trap density reduces the quantum efficiency and this decrease is relatively small until the trap concentration approaches the order of magnitude of the dopant concentration [9]. Physical experiments have also shown a degradation in quantum efficiency due to radiation-induced traps [44] [45].

As Figures 10 and 11 are the results of computer modeling, they represent trends that would be measured under ideal conditions. To test how well these trends apply to other detectors such as the photodiodes studied in this work, DLTFS measurements may be used to measure trap concentrations and CV data may be used to calculate the carrier depth profile of the samples.

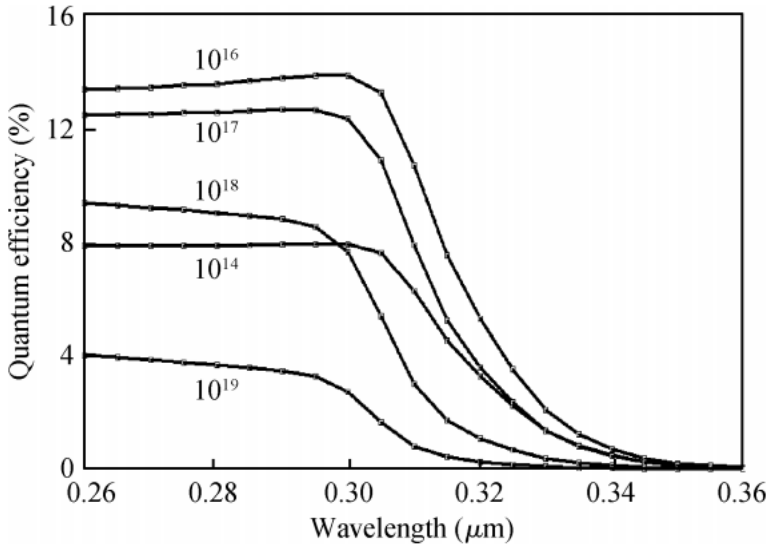

Figure 10. Dopant effect on quantum efficiency for a simulated Schottky AlGaN detector. Reproduced with permission from [9].

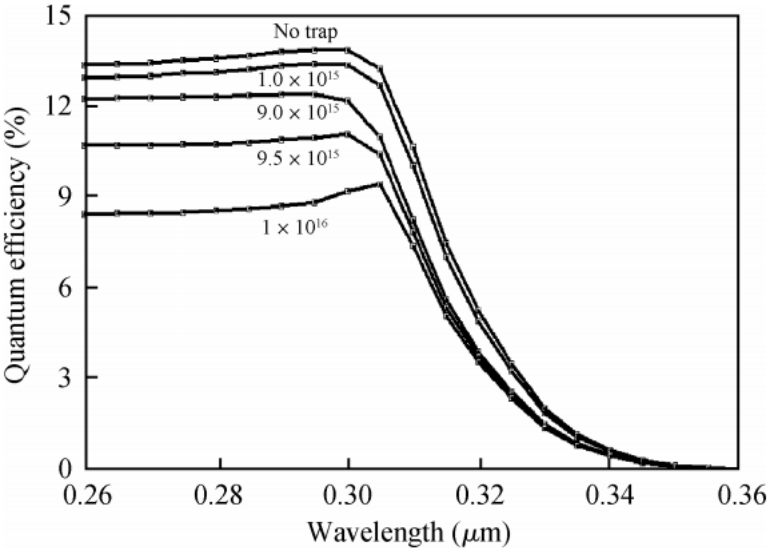

Figure 11. Trap concentration effect on quantum efficiency for a simulated Schottky AlGaN detector. The doping concentration is equal to 10^{16} cm^{-3}. Reproduced with permission from [9].

2.4 Deep-Level Transient Fourier Spectroscopy

Deep-level transient Fourier spectroscopy (DLTFS) is an adaptation of the conventional deep-level transient spectroscopy (DLTS) method, so conventional DLTS will be explained first to show how DLTFS differs.

DLTS uses a thermal scan of the capacitance transient in a semiconductor to create a spectrum that can be used to determine the concentration, activation energy, and electron/hole-capture cross section for deep-level defects [10]. Figure 12 models the process used to measure a minority carrier trap.

A reverse-biased junction can be modeled as a parallel plate capacitor [39], so its capacitance, C, is given by:

$$C = \frac{K_s \epsilon_0 A}{W}, \tag{5}$$

where K_s is the semiconductor dielectric constant, ϵ_0 is the permissivity of free space, A is the surface area of the junction, and W is the width of the depletion region of the junction. The width of the depletion region grows with greater reverse bias and shrinks with greater forward bias, so the capacitance of the diode can also be expressed as a function of voltage [39]:

$$C(V) = A\sqrt{\frac{qK_{s0}}{2}}\sqrt{\frac{N_{dep}}{V_{bi} - V}}, \tag{6}$$

where q is fundamental charge of an electron, N_{dep} is the ionized impurity density in the depletion region, V_{bi} is the built-in potential of the diode, and V is the applied bias.

As shown in Figure 12, at a sufficient reverse measurement bias, the traps in the depletion region of the photodiode are emptied. A forward bias is applied to shrink the depletion region and allow carriers to fill the traps that can function as recombination-generation centers. This consequently increases the capacitance of the

diode. When the bias is returned to the measurement bias, the carriers can no longer cross the energy band gap and return to the band from which they came. This causes an exponential decay of the capacitance that is measured through time [10] and given by [39]:

$$C(\infty) - C(t) = \frac{N_T(0)}{2N_D} C_0 \exp\left(\frac{-t}{\tau_e}\right), \tag{7}$$

where N_T is the trap density, N_D is the dopant density, and τ_e is the emission time constant.

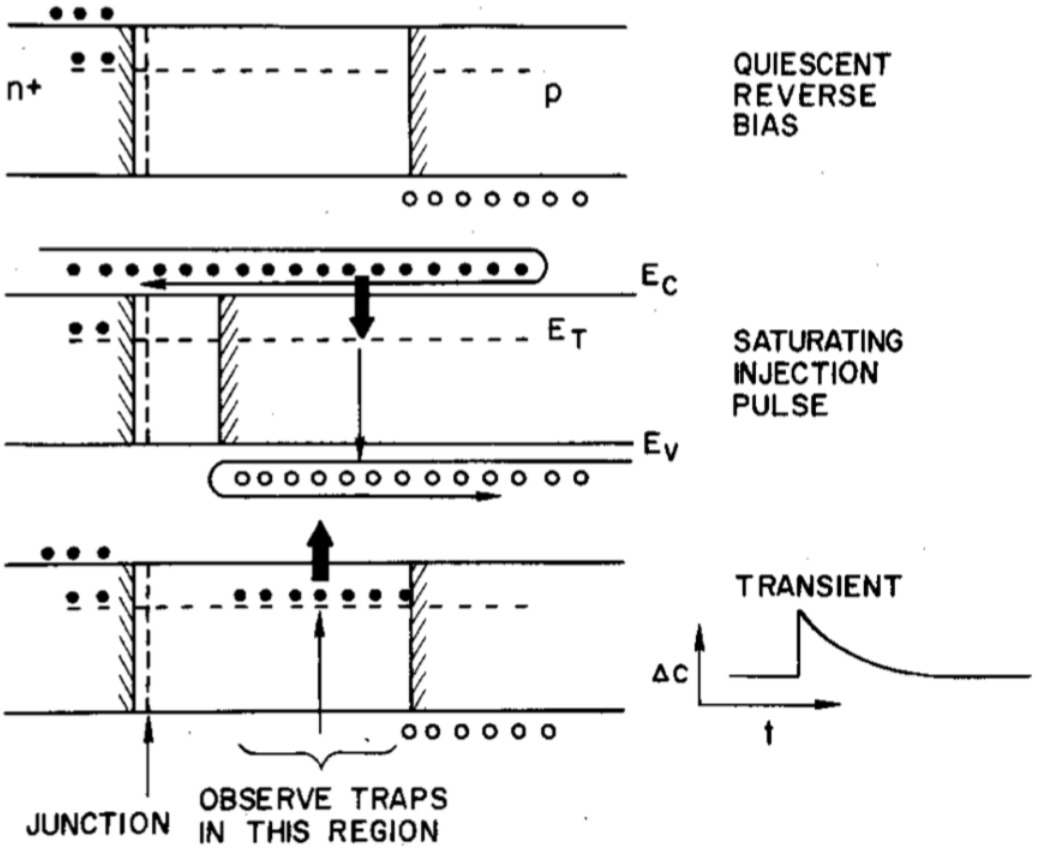

Figure 12. Steps to measure a minority-carrier trap. At measurement reverse bias, traps are empty. Fill voltage pulse is injected to fill traps and increase the capacitance. Voltage is returned to measurement reverse bias and change in capacitance is measured as traps are emptied. Reproduced with permission from [10].

Note that Figure 12 shows this process for an n^+p diode which is a p-type mate-

rial whose minority carriers are electrons. The same capacitance transient would be observed for an n-type material in which holes are the minority carriers. However, in either case, if a majority carrier trap were filled by the pulse bias, a decrease in capacitance would be measured followed by an increase in capacitance back to the pre-pulse level. Thus, on a DLTS spectrum, a positive peak indicates a minority carrier trap and a negative trough indicates a majority carrier trap whether the semiconductor measured is n-type or p-type [10].

Two conditions must be fulfilled for successful capacitance transient measurements. The first is that the capacitance of the semiconductor must vary predictably with voltage. In the ideal case, the C-V curve will increase gradually as reverse bias approaches zero, then peak at a forward bias not much greater than 0 V [46]. This provides a strong and easily measurable transient. The second condition is that the reverse bias should suppress the leakage current to a minimum. If the leakage current is not suppressed, the defects will continue to act as recombination-generation centers, and the capacitance transient will not be clear [47].

Figure 13 shows that the capacitance transient is also a function of temperature and the rate window used to observe the capacitance change. The rate window is simply the time interval between the points at which capacitance of the semiconductor is recorded the first and second time. As temperature increases, the charge carriers move faster and the emission time constant is reduced according to the equation [39]:

$$\tau_e = \frac{\exp\left(\frac{E_i - E_T}{kT}\right)}{\sigma v_{th} n_i}, \tag{8}$$

where E_i is the intrinsic mid-band gap energy level, E_T is the defect energy level, k is the Boltzmann constant, T is temperature, σ is the carrier capture cross-section, v_{th} is the carrier thermal velocity, and n_i is the intrinsic carrier density. The maximum capacitance transient is measured when the carrier emission rate (the inverse of τ_e)

is on the same order as the rate window. It can be shown that the corresponding emission time constant, τ_{max} is therefore determined by the rate window [10]:

$$\tau_{max} = \frac{t_1 - t_2}{\ln\left(\frac{t_1}{t_2}\right)}. \tag{9}$$

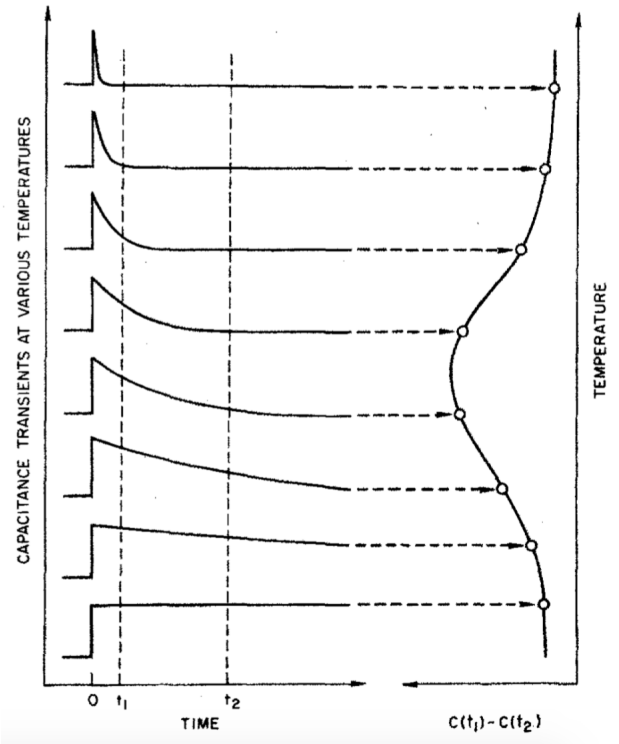

Figure 13. Change in the capacitance transient observed for a given measurement window between t_1 and t_2 as temperature increases. Reproduced with permission from [10].

The defect concentration, N_T can be found from the capacitance change resulting from complete trap filling by [10],

$$N_T = 2(N_A - N_D)\frac{\Delta C}{C}, \tag{10}$$

where $N_A - N$ is the net acceptor concentration in the part of the junction where the defect is observed, ΔC is the capacitance change at time zero when the fill bias was

applied, and C is the capacitance of the diode at the measurement reverse bias. To assure that the traps are completely filled, the pulse of fill bias may be lengthened until the peak on the DLTS spectrum does not increase any more in size. Because the first capacitance measurement is taken some time after the pulse is applied, ΔC is determined by [10],

$$\Delta C = \frac{[C(t_1) - C(t_2)]}{[\exp(\frac{-t_1}{\tau_{max}}) - \exp(\frac{-t_2}{\tau_{max}})]}. \tag{11}$$

The DLTS thermal scan can be repeated for different rate windows as shown in Figure 14. For each rate window, the peaks give temperature and emission time constant values that can be used to make an Arrhenius plot. According to Equation 8, if the natural log of the time constants are plotted verses 1/T, the slope of the resulting line will be $\frac{E_i - E_T}{k}$ from which the defect energy level can easily be calculated. If the intrinsic carrier density and thermal velocity are known, the carrier capture cross-section can also be calculated from the y-intercept of the Arrhenius plot [10].

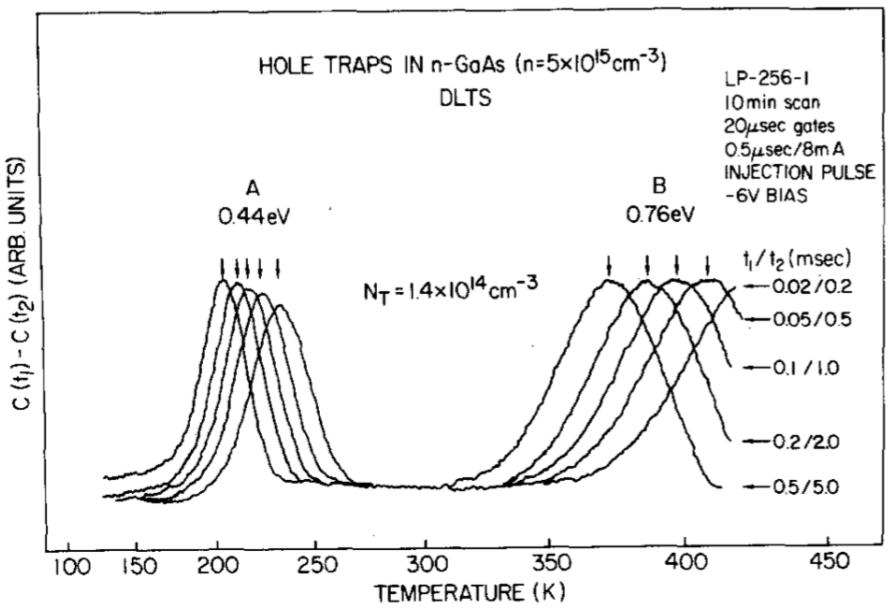

Figure 14. DLTS spectra of hole traps in n-type GaAs with rate windows varying from 0.18 ms to 4.5 ms. Reproduced with permission from [10].

The disadvantage of the conventional DLTS method is that it is time-consuming because each DLTS spectrum measured only yields one point of the Arrhenius plot needed to determine the defect energy level. The DLTFS method avoids this problem by sampling N values of a capacitance transient, then uses a numerical Fourier transformation to create N Fourier coefficients. If the capacitance exponential decay function is expressed by [48]:

$$f(t) = Aexp[\frac{-(t+t_0)}{\tau}] + B, \tag{12}$$

where A is the amplitude, B is the offset, and t_0 is the time at the end of the fill voltage pulse, then the Fourier coefficients are given by [48]:

$$c_n = \frac{1}{T_w}\int_0^{T_w} f(t)\exp(-in\omega t)dt, \tag{13}$$

where T_w is the rate window and ω is the period,

$$\omega = \frac{2\pi}{T_w}. \tag{14}$$

The Fourier coefficients are made up of real and imaginary parts,

$$c_n = \frac{1}{2}(a_n - ib_n), \tag{15}$$

where a_n and b_n are in turn defined by the exponential decay parameters [48]:

$$a_n = \frac{2A}{T_w}\exp(\frac{-t_0}{\tau}) \times [1 - \exp(\frac{-T_w}{\tau})]\frac{\frac{1}{\tau}}{\frac{1}{\tau^2} + n^2\omega^2}, \tag{16}$$

$$b_n = \frac{2A}{T_w}\exp(\frac{-t_0}{\tau}) \times [1 - \exp(\frac{-T_w}{\tau})]\frac{n\omega}{\frac{1}{\tau^2} + n^2\omega^2}. \tag{17}$$

Manipulation of these equations allows three possibilities to determine τ from the measured a_n and b_n values [48]:

$$\tau(a_n, a_k) = \frac{1}{\omega}\sqrt{\frac{a_n - a_k}{k^2 a_k - n^2 a_n}}, \tag{18}$$

$$\tau(b_n, b_k) = \frac{1}{\omega}\sqrt{\frac{kb_n - nb_k}{k^2 nb_k - n^2 ka_n}}, \tag{19}$$

$$\tau(a_n, b_n) = \frac{1}{n\omega}\frac{b_n}{a_n}. \tag{20}$$

All of these coefficients are created at each temperature the capacitance transient is measured. As in the conventional DLTS method, a thermal survey of the capacitance transient is taken to create a spectrum like those shown in Figure 14. From these measurements, N spectra are created by plotting the Fourier coefficients against temperature. Analogous to the peak shift of the conventional DLTS spectra with changing rate windows, the DLTFS spectrum peaks shift as the order of the

Fourier coefficients increase. An Arrhenius plot can be constructed by plotting these max τ values versus temperature in the same way as described for the conventional DLTS method. Although it is implied that N points of the Arrhenius plot can be extracted from each peak of the DLTFS spectrum, the Fourier coefficients converge as n increases, so there is an upper limit to the number of coefficients that can extract useful data dependent on the size of T_w. Usually this is on the order of tens of data points. The three different methods used to calculate τ shown above result in slightly different Arrhenius plots, so they serve as a measure of the uncertainty of the defect energy level and carrier capture cross-section determined from the plots [48].

III. Methodology

3.1 Sample Properties

The samples used in this study were produced at Arizona State University and provided by Professor John Kouvetakis of the School of Molecular Sciences. The fabrication process started with a germanium-buffered silicon substrate [19] which had a SiO_2 protective layer applied to it about 100 nm thick. Then photolithography was used to set up the pattern of mesas that would be the basis of the device structures. The mesa diameters in these samples ranged from 120 to 2740 μm. After chemical rinsing of the samples, the chemical vapor deposition (CVD) technique was used to grow the GeSn layers on top of the germanium-buffered silicon substrate. Photolithography was used again to define the metal contact regions surrounding the p-i-n mesas needed for probing. A 20 nm layer of chromium was then deposited in the defined contact region followed by a 190 nm layer of gold. Finally, the samples were polished and chemically rinsed again to optimize their optical performance [17]. A schematic of the general p-i-n structure is shown in Figure 15. Specific schematics of the different sample types are provided in the appendix.

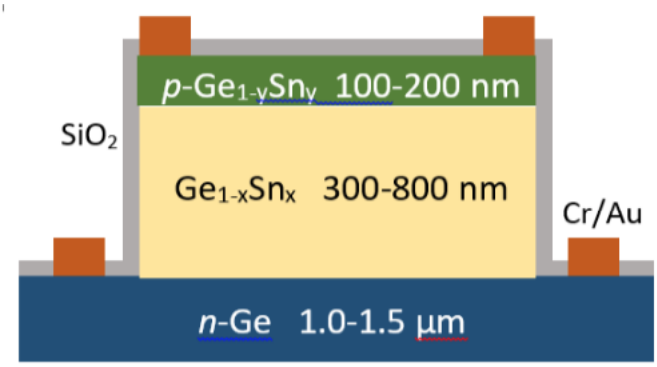

Figure 15. Schematic of p-i-n hetero-structure, not to scale [11].

The p regions of the diodes were doped with between 7.9×10^{18} cm^{-3} and 5.2×10^{19}

cm^{-3} boron atoms while the n regions were doped with between 1.8×10^{19} cm^{-3} and 2.8×10^{19} cm^{-3} phosphorous atoms. The unintentional doping level of the intrinsic regions ranged from 5×10^{16} to 2×10^{17} cm^{-3}. The 0% tin devices were grown as n-type p-i-n junctions while the rest of the devices were grown as p-type. The major properties of the intrinsic regions are given in Table 1.

3.2 Irradiation Conditions

The neutron source for the irradiation was the research reactor at the Ohio State University (OSU), pictured in Figure 16, which has a maximum operating output of 450 kW thermal. The OSU reactor has a variety of tubes in and around the core that serve as irradiation facilities. The neutron flux in these facilities has been measured using the neutron foil activation method [49]. Because the energy of neutrons produced by the reactor is not constant, it is necessary to use 1 MeV equivalent neutron flux values, which is the standard method to allow comparison of radiation damage from different neutron sources. These values have been calculated for the OSU irradiation facilities in accordance with standards produced by the American Society for Testing and Materials. The pneumatic "rabbit tube" facility was used in this study because of the convenient and quick access it allowed to insert and remove samples to and from the neutron field. As shown in Figure 16, the rabbit tube places the samples adjacent to the reactor. At max operating power, the 1 MeV (Si) equivalent neutron flux in the rabbit tube is $5.6 \times 10^{11} cm^{-2} s^{-1}$ [49].

Figure 16. Overhead view of Ohio State University nuclear reactor. The curved tube is the pneumatic "rabbit tube" facility used in this study.

For the irradiation, the samples were cut into pieces of approximately 25 mm^2 area. Although they would later be packaged and wire-bonded to facilitate DLTFS measurements, it was necessary to irradiate only the bare samples to limit the amount of sample activation. To mitigate the effect of room-temperature annealing, dewers filled with liquid nitrogen were used to store the samples post-irradiation. However, it was necessary to leave the samples behind radiation shielding for a period of time to allow the short-term activation radiation to cool down. If the samples had been packaged during irradiation, the activation radiation and wait-time for cooling would have been an order of magnitude greater.

The samples were divided into four groups based on irradiation time: a control group, a low-fluence group, a medium-fluence group, and a high-fluence group. Each group contained one sample from each of the five diode types described in Table 1. These groups were packed with cotton padding in the polyethylene bottles pictured in Figure 17 for transport through the rabbit tube. To mitigate timing error, for

the low-fluence group, the nuclear reactor was brought to 45 kW output. For the medium and high-fluence groups, it was brought to 450 kW. Table 2 summarizes these radiation conditions.

Figure 17. Containers used to transport sample groups through rabbit tube for irradiation.

Table 2. Irradiation conditions of sample groups. Each group contains a sample of 0%, 2%, 5.3%, 6.8%, and 6.9% diode types.

Group	Reactor Power (kW)	Radiation Time (s)	Cool Time (s)	Fluence (cm^{-2})
1	0	0	0	0
2	45	76	60	4×10^{12}
3	450	76	600	4×10^{13}
4	450	755	3600	4×10^{14}

3.3 IV Curve Measurements

Figure 18 illustrates the setup used to make the IV curve measurements. As shown in Figure 19, each sample contained a variety of p-i-n devices with mesa diameters ranging from 120 to 2740 μm. In this study, the 580 μm were used for all measurements because they were the smallest devices that could feasibly be probed consistently and accurately. Measuring the smaller devices was desirable to mitigate

the possibility of inhomogeneity in the p-i-n device being measured.

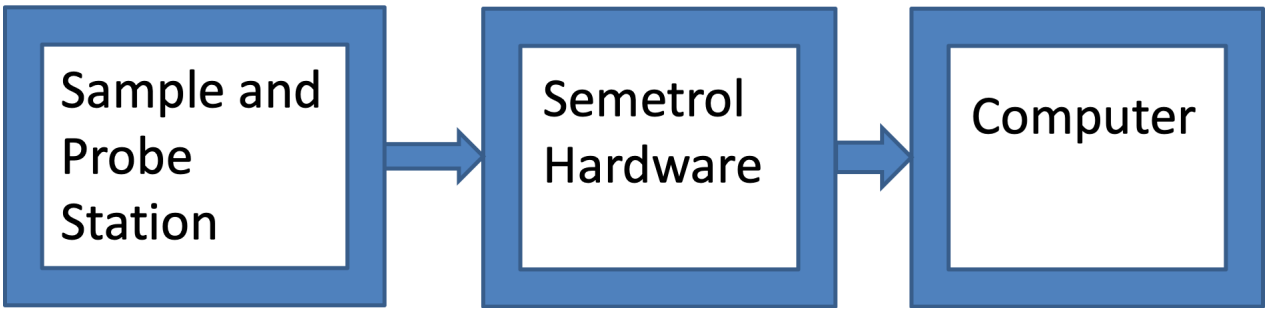

Figure 18. Experimental setup for IV curve measurements. Semetrol, LLC, produces semiconductor characterization equipment.

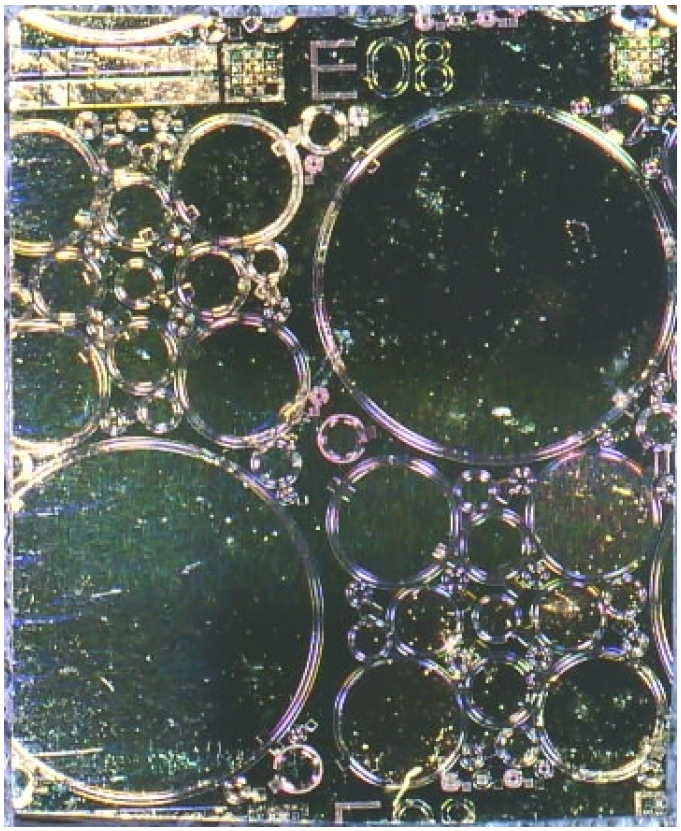

Figure 19. Photograph of GeSn sample. Mesa diameters range from 120 to 2740 μm. Probes were applied to the gold, metallized region for experimental measurements.

The IV curves were measured from -0.6 to 0.4 V to observe how well the devices demonstrated ideal rectifying behavior while avoiding high voltages that could damage

the diodes. Initial measurements showed a large variation of IV curve results among diodes measured from the same sample. While some had good rectifying behavior with the reverse bias current 1000 times lower than the forward bias current, many others showed a decrease of only a factor of 10. For this reason, five to eight devices were measured on each sample to find the samples with the best rectifying behavior to be used for the DLTFS measurements. The same devices were measured before and after irradiation for direct comparison.

3.4 Photoresponse Measurements

Photoresponse measurements were taken at zero bias, so it was necessary to amplify the response. To suppress noise, a function generator was used to pulse the 455 nm blue light that shined on the diodes and this function was also input to a lock-in amplifier. This type of amplifier uses phase-sensitive detection to compare a reference function to an oscillating signal. This produces a measurement of the output voltage:

$$V_{psd} = \frac{1}{2} V_s V_r \cos \theta_s - \theta_r, \tag{21}$$

where V_{psd}, V_s, and V_r are the phase-sensitive detector, signal, and reference amplitudes, respectively, and θ_s and θ_r are the corresponding frequencies [50]. Although this method does not directly measure the current produced by photoresponse, it does provide a relative measure that was appropriate for the scope of this study and its goal of observing the change in behavior due to radiation. Figure 20 illustrates the setup used to make the photoresponse measurements and Figure 21 is a photo of the laboratory setup. The settings for the equipment used in this study are summarized in Table 3.

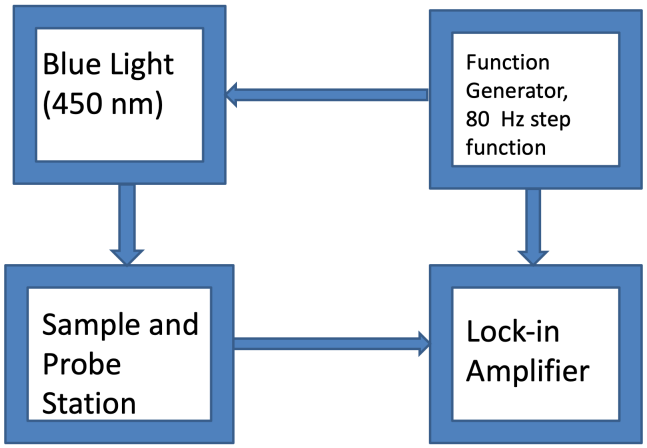

Figure 20. Schematic of equipment setup for photoresponse measurements.

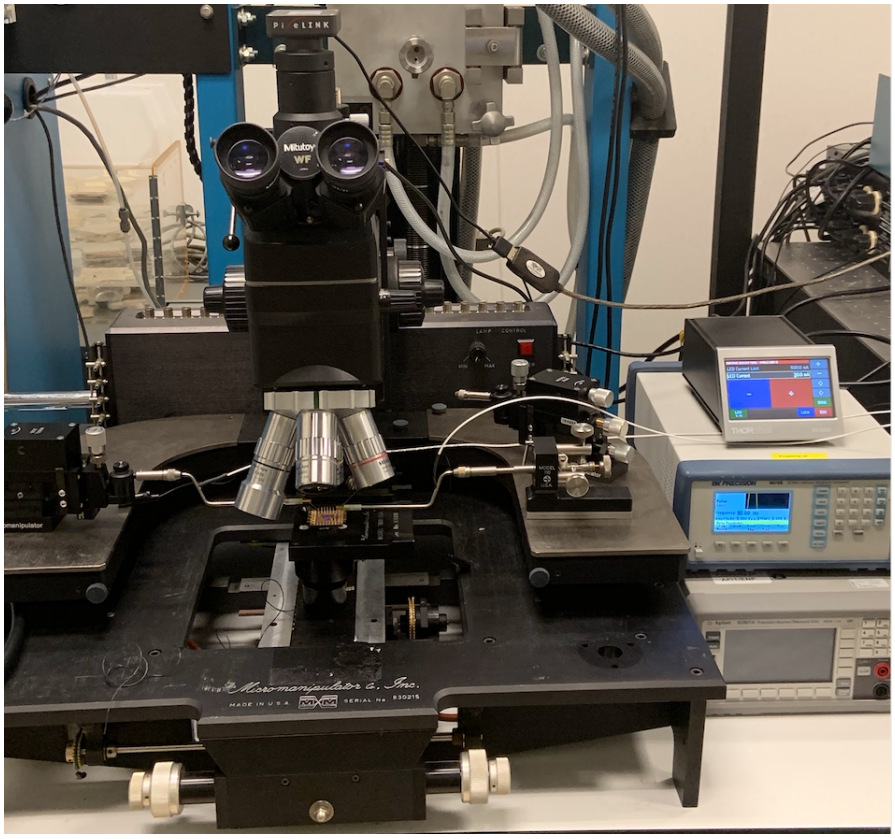

Figure 21. Probe station used to make photoresponse measurements. Light shined on samples through the top of the microscope. LED driver and function generator are to the right of the microscope. Lock-in amplifier not pictured.

Several devices were measured on each sample as was done for the IV measurements, but the photoresponse had much lower variance, ranging by 5% to 10% for

Table 3. Equipment and settings used for photoresponse measurements.

Component	Manufacturer	Model #	Serial #	Notes
High-Power 1-Channel, LED Driver	Thor Labs	DC2200	M00422528	Pulse mode fed by function generator
Mounted 455 nm Wavelength LED	Thor Labs	M455L3	M00325350	Light 30 cm above photodiode
Arbitrary Wavelength Generator	BK Precision	4075B	453F150003	Step function: Frequency = 80 Hz Amplitude = 5 V
Digital Lock-in Amplifier	Stanford Research Systems	SR850	87015	Reserve = 30 dB Filtering = 24 dB/oct

devices of the same diode type. For this reason, the irradiated samples could be compared to the control samples to measure the change in photoresponse due to radiation.

3.5 DLTFS Measurements

DLTFS measurements were collected with Dr. Buguo Wang at the semiconductor characterization lab at Wright State University. The DL8000 DLTFS system produced by Accent Optical Technologies was used with a small cryogenic chamber cooled by liquid nitrogen to make transient capacitance measurements from 85 K to 290 K. Good measurements are dependent on a stable capacitance-voltage (CV) relationship, which is generally better at low temperatures. While many samples were successfully measured up to 290 K, some measurements had to be stopped at lower temperatures.

Although measurements were initially made by probing the bare samples, the low temperature of the DLTFS process sometimes caused movement of the probes off the p-i-n contacts and failure of the measurement. To achieve more consistent results, after all IV and photoresponse measurements had been made, the samples were packaged and wire-bonded as shown in Figure 22.

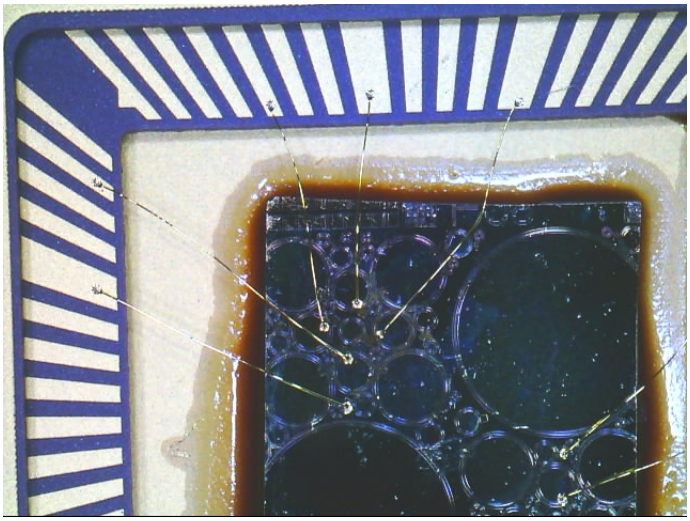

Figure 22. Samples were mounted on 76-pin packages and metallized diode nodes were gold wire-bonded in preparation for DLTFS measurements.

There were four main measurement parameters that were adjusted for the measurements: measurement voltage, fill voltage, rate window, and pulse width. The measurement voltage is ideally set to a reverse bias so that the leakage current is low. Because the reverse bias current of the samples used in this study were relatively high, the magnitude of the reverse bias was usually set quite low, ranging from 0 to 0.3 V. Occasionally successful measurements could be made at a reverse bias as great as 1 V. In theory, the fill voltage is optimal where the CV relationship peaks [47], but if the magnitude is too high, majority and minority defects may be detected on the same temperature scan spectrum which is not optimal for defect characterization. To mitigate this effect, measurements were taken with the fill voltage varying between 0 and 0.5 V, forward bias.

Although the advantage of the DLTFS method is that it numerically simulates different rate window temperature scans, it is good practice to repeat measurements for different rate window values to make sure observed trends are repeated. Measurements were taken with the rate window varying between 4 and 200 ms. The pulse width is the amount of time the fill voltage is applied for each capacitance transient

measurement. It was generally set to 10 ms, but was occasionally varied between 1 and 100 ms.

IV. Results and Analysis

4.1 IV Curve Results

Systematic analysis of the IV curve measurements is challenging due to the large variance of behavior among devices on the same sample and with the same tin content. The expected trend for IV curves with radiation damage was an increase in dark current for reverse bias and a decrease in dark current for forward bias [2]. Only 18 of the 89 devices measured showed this specific behavior; an example is shown in Figure 23. 26 of the devices showed a decrease in the forward bias current only. Although this was not accompanied by the expected increase in reverse bias current, it was expected, so we may say that 44 of the devices had normal post-radiation degradation of rectifying behavior. 23 of the devices had an increase in current for forward and reverse bias. An example of this is behavior is given in Figure 24. 13 devices had an overall decrease in current while 9 had no notable change. Overall, a little more than half of the devices had an unexpected post-irradiation change.

IV curve results also revealed that many of the diode devices had poor rectifying behavior as grown. For example, Figure 23 shows that the reverse bias dark current was less than a factor of ten lower than the forward bias current. As in previous studies [11] [17], the dark current was generally worse as the tin content was increased, but diodes with IV curves similar to Figure 23 were found in all samples. Figure 24 is an example of one of the best sample's rectifying behavior. Because low dark current is necessary for good DLTFS measurements [47], the devices with the best rectifying behavior were used for DLTFS measurements.

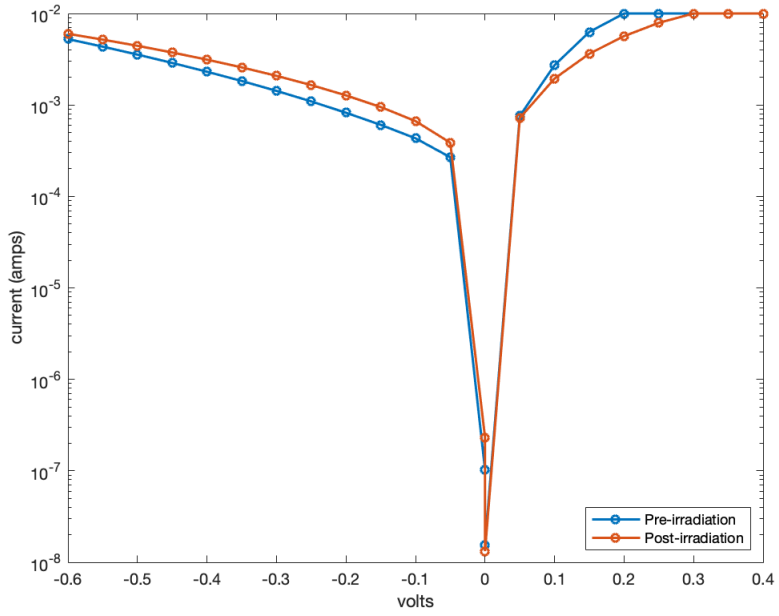

Figure 23. IV curve of one 6.9% Sn diode subject to $4 \times 10^{14}\,\mathrm{cm}^{-2}$ neutron fluence.

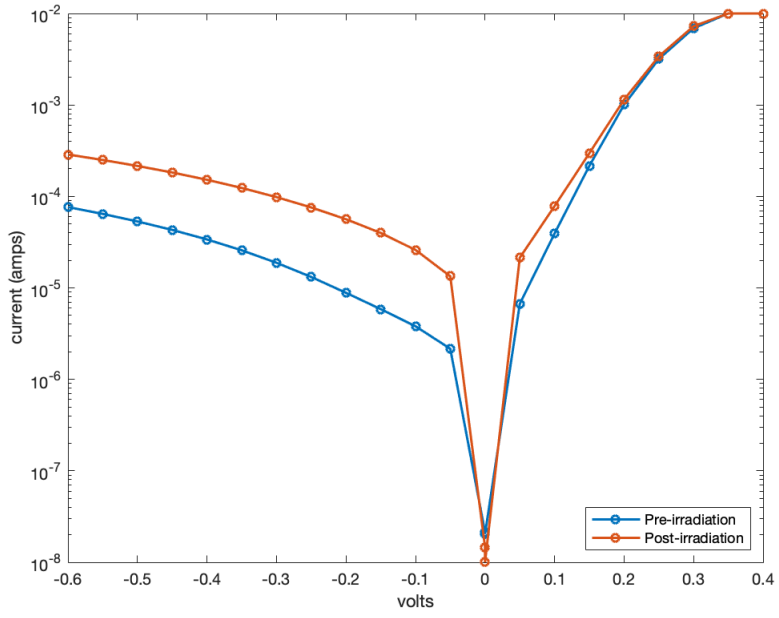

Figure 24. IV curve of one 2% Sn diode subject to $4 \times 10^{12}\,\mathrm{cm}^{-2}$ neutron fluence.

Figure 25 shows that although all diode types were represented by a variety of post-irradiation IV curve changes, some changes were more common than others based

on tin content. While the majority of devices of high tin content had the expected behaviors, the low tin samples were more prone to an overall increase in current for both reverse and forward biases.

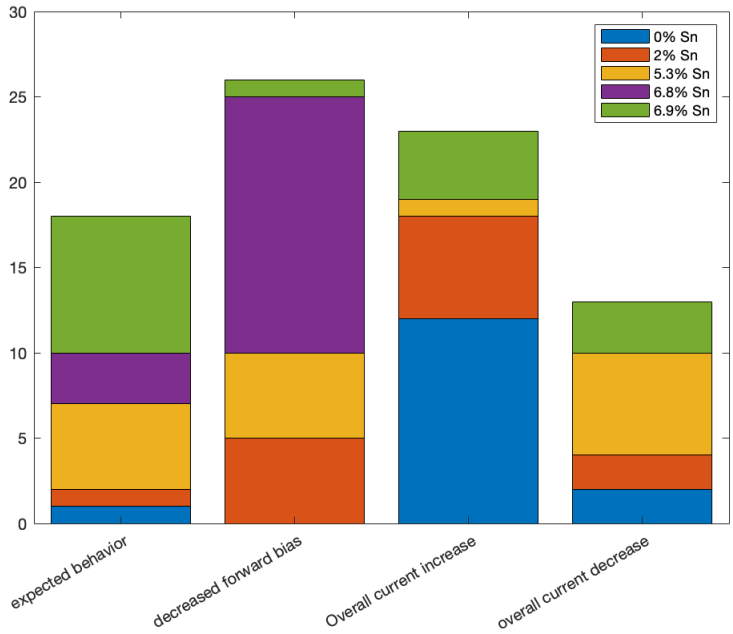

Figure 25. Photodiode devices grouped by the radiation effects on their IV curve.

A particularly surprising result, represented in Figure 26, was that there was no clear correlation between the change in reverse-bias dark current and neutron fluence. In fact, two out of five of the diode types showed their greatest change for the low fluence samples. Although the low fluence 0% Sn sample and the 6.9% mid and high fluence samples appear to have much greater post-irradiation change in dark current than the other samples, the uncertainty of these measurements is very large. Therefore, no statistically significant trend can be extracted relating post-irradiation change in dark current to tin content or neutron fluence.

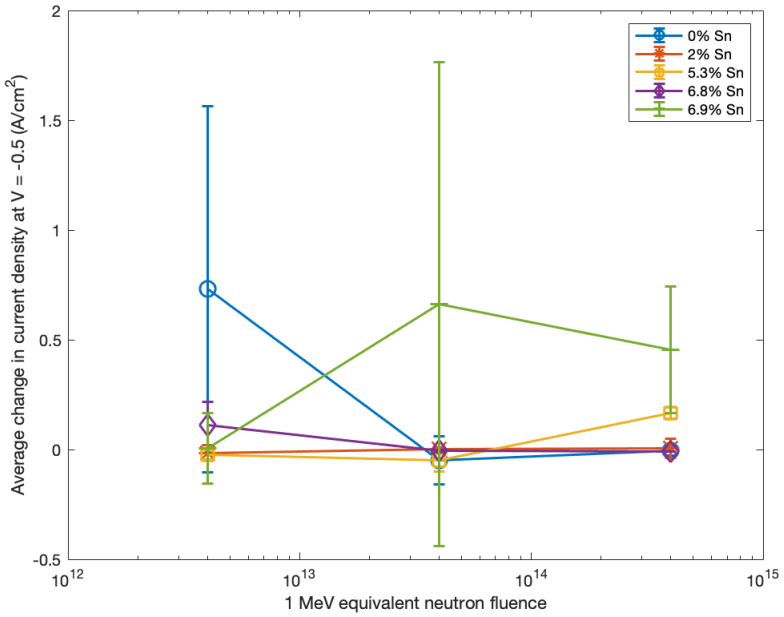

Figure 26. Average change in current density at -0.5 V reverse bias.

The large variance in IV curve results and the large dark current in the majority of devices measured are not surprising because the samples used in this study were produced in a laboratory setting. The growth method was not subject to major quality control measures, so it was not expected that all devices would have ideal rectifying behavior. Nevertheless, enough measurements were taken to conclude with some confidence that the high tin content samples generally had greater dark current than the low tin content samples. Past experiments have shown that high tin content samples tend to start with high initial defect densities [11] [17] which causes them to have an increased dark current. This may be caused in part because the larger size of the tin atoms make lattice deformations like stacking faults more likely than in a uniform germanium lattice.

4.2 Photoresponse Results

Figures 27 through 31 show the increased lock-in amplifier reading as the incident light intensity was increased from 50 mA to 1000 mA for all samples. Again, these results are contrary to expectation as all irradiated samples yielded better photoresponse than the control samples. The same diode types that had the greatest IV curve change in the samples subject to the low neutron fluence level also had the greatest photoresponse increase in the low fluence samples. However, unlike the IV curve results, for these diode types there is a clear trend related to the fluence level. In Figures 27, 28, and 30, it can be seen that as fluence increases, the increase in photoresponse is reduced.

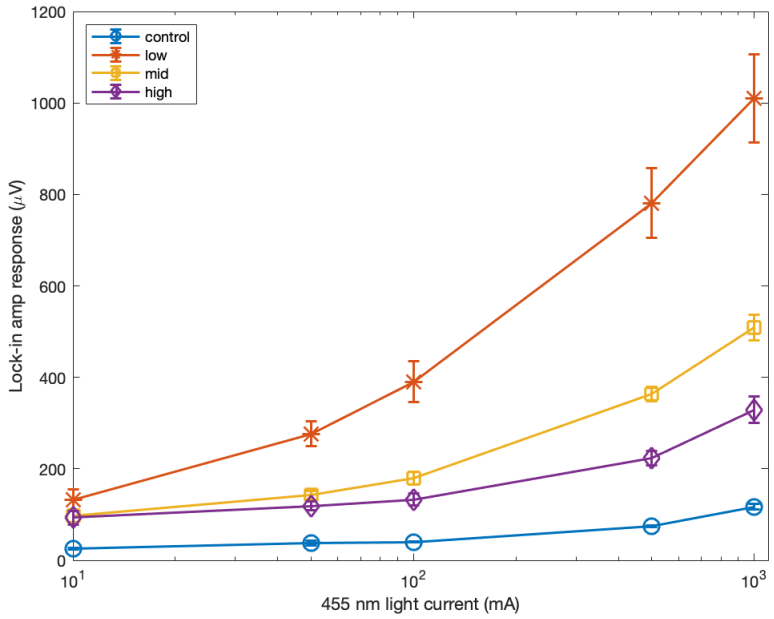

Figure 27. 0% Sn photoresponse as a function of increased incident light intensity.

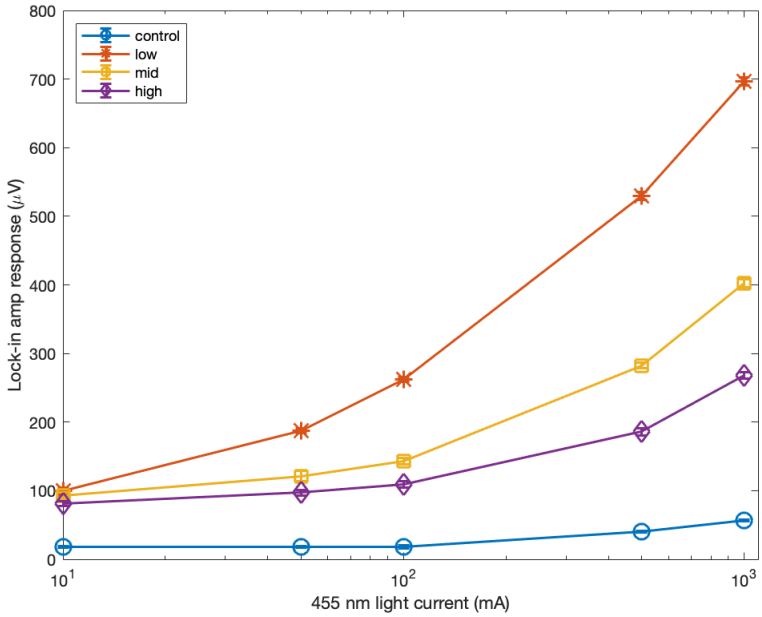

Figure 28. 2% Sn photoresponse as a function of increased incident light intensity.

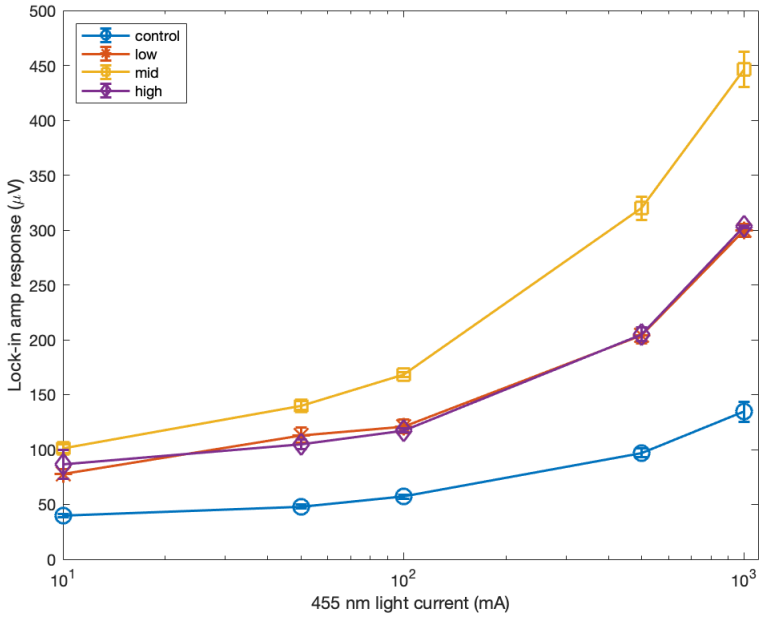

Figure 29. 5.4% Sn photoresponse as a function of increased incident light intensity.

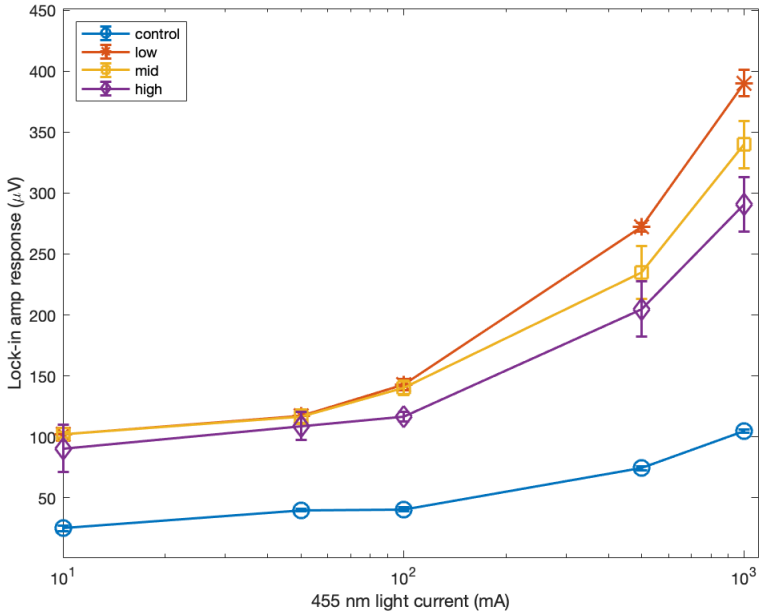

Figure 30. 6.8% Sn photoresponse as a function of increased incident light intensity.

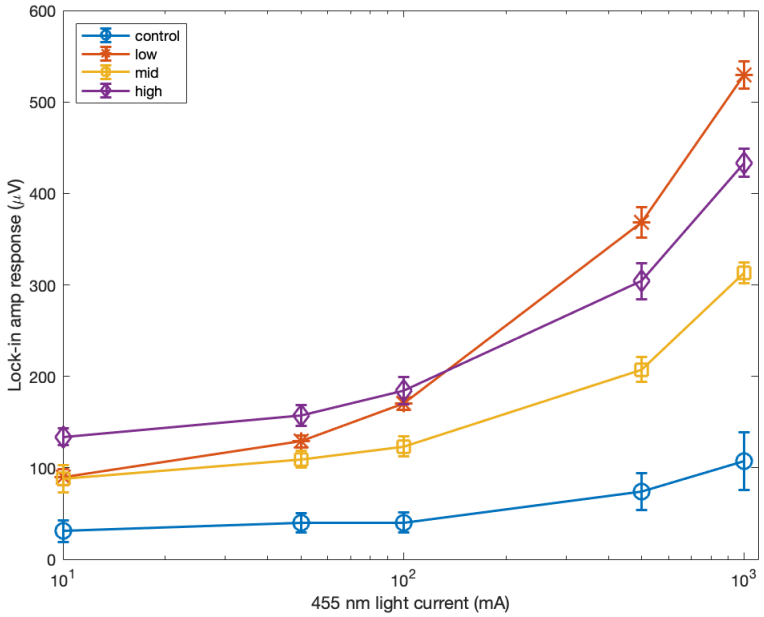

Figure 31. 6.9% Sn photoresponse as a function of increased incident light intensity.

Figure 32 directly compares the change in photoresponse for all diode types by graphing the percent increase in the response reading when compared to the ap-

propriate control sample at the highest incident light intensity measured, 1000 mA. Although Figure 27 shows that the 0% Sn sample had the greatest photoresponse reading, the 2% Sn sample had the greatest increase (more than a factor of ten). In general, we see that the samples with high tin content tended to have a less dramatic increase in response than the samples of low tin content. It is notable that the 6.8% and 6.9% Sn samples had considerably different responses to irradiation given that they have the most similar intrinsic region properties. This discrepancy is likely due to the differences in the size and doping properties of the p and n regions that can be seen in the appendix.

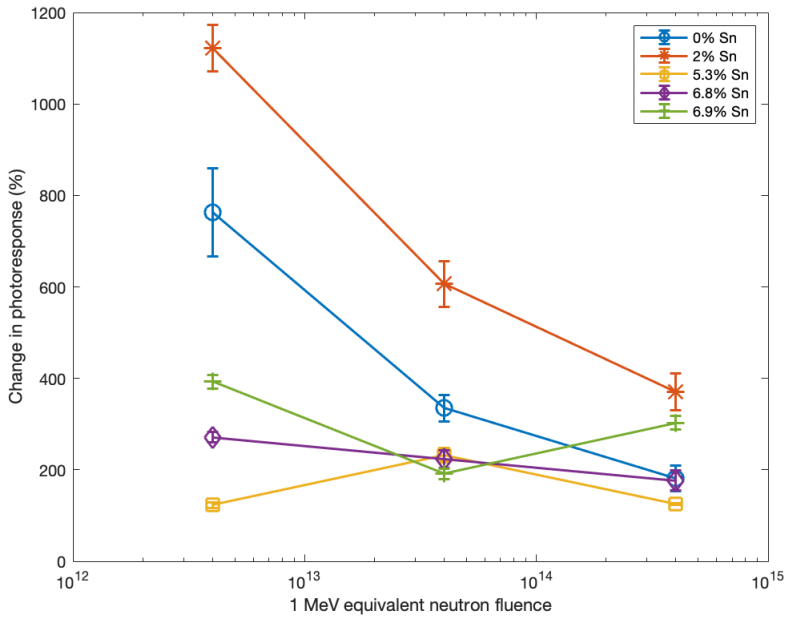

Figure 32. Percent increase in photoresponse post-radiation as compared to control samples. Measurements taken at 1000 mA incident light intesity.

Figure 32 suggests that for these diodes, there is an optimal, low-level of radiation fluence that maximizes the photoresponse. In the majority of the diode types, increased radiation caused a decrease in photoresponse relative to the low fluence samples. That is, after the initial boost due to low fluence, the sample's response

began to degrade as the radiation created defects in greater concentrations. This decrease seen in the mid and high fluence samples was what was initially expected for all samples, and is in accordance with the behavior predicted by Figure 11. This decrease is caused by the recombination-generation centers in the intrinsic region.

Although the 5.3% tin samples had a slightly different pattern (the sample subject to the mid level of fluence had the greatest photoresponse), it still supports the hypothesis that there is an optimum level of radiation that improves the photoresponse, although the reason that this level was higher for the 5.3% Sn samples than the others is unknown. In contrast, the 6.9% tin samples do not fit this explanation because the low fluence sample had the greatest photoresponse, followed by the high fluence sample, and finally the mid-fluence sample. However, as mentioned, the magnitude of increase was not as great for this sample as it was for the low tin content samples, so it is possible that this discrepancy in the trend is due to the statistical uncertainty of defect creation due to neutron irradiation.

The mechanism that causes the increase in photoresponse post-irradiation is unknown. Underdoping is one possible explanation for the increased photoresponse measured in the samples. Although Figure 11 shows that the quantum efficiency of the photodiodes is expected to decrease with increasing trap concentration, that assumes that the diode started at its optimum dopant level. Figure 10 shows an increase of almost 75% when the dopant concentration was increased from $10^{14}\,\mathrm{cm}^{-3}$ to $10^{16}\,\mathrm{cm}^{-3}$, then a decrease of similar magnitude for a dopant concentration of $10^{18}\,\mathrm{cm}^{-3}$. Based on Figure 32 it appears that the low level of radiation in the samples may have caused dopant compensation, bringing the diodes to a more favorable dopant level than the as grown samples. However, as shown below, this hypothesis is not supported by the carrier depth profile calculated from the CV curve measurements. It is possible that dopant compensation is a major factor in parts of the

p-i-n samples where the carrier depth profile could not be measured, but there is no evidence to support this idea.

Although the results of improved, post-irradiation photodiode behavior were unexpected, this type of result is not entirely unprecedented. As mentioned above, Choe measured photoluminescence (a distinct but related phenomenon to photoresponse) in GeSn samples before and after proton irradiation. Unlike this study, Choe observed improvement in only a limited number of samples, all with 9.4% tin content [11]. At least part of the reason for this discrepancy is likely due to the difference in radiation source used. As shown in Figure 9, the 2 MeV protons Choe used have a NIEL value more than ten times as great as the 1 MeV neutrons used in this study. The protons created many more defects, so even the samples subject to the low proton fluence level (also $4 \times 10^{12}\,\mathrm{cm}^{-2}$) had many more traps created than would be beneficial. It is plausible that the only sample that had a low enough level of trap creation was the 9.4% tin because the high tin content made the sample less susceptible to radiation damage.

Blansett also observed improved responsivity for photodiodes subject to neutron irradiation, but unlike this study in which the irradiated samples' photoresponse was many times greater than the control samples', the improvement was below 10% in all cases [22]. There are likely two reasons for this discrepancy. The first is that photodiodes from several commercial semiconductor manufacturers were used, so the quality control would have been much greater than the laboratory-produced samples used in this study. The second reason is that Blansett made the responsivity measurements at a 1 V reverse bias while zero bias was used for the responsivity measurements in this work. At zero bias, the electrical signal from the photodiode was extremely small, so a small absolute change resulted in a large percent change.

Finally, the results also support the conclusion that increasing the tin content of

the diodes makes them less sensitive to radiation damage. This is because the greater mass of tin atoms make them less likely to be knocked out of position by neutrons than germanium atoms and because the smaller band gap due to the higher tin content reduces the relative importance of recombination-generation centers in charge carrier band transitions. The drawback is that tin has considerably greater size than germanium which causes more lattice deformations than in pure germanium. These factors imply that although photodiodes with high tin content may be less sensitive to radiation effects, they have high dark current and poor rectifying behavior which is problematic for detection and imaging applications.

4.3 CV Curve Results

As mentioned above, CV curve measurements are used to calculate the carrier depth profile of the depletion region of p-n and p-i-n junctions which is one way to test the dopant compensation explanation of improved post-irradiation photoresponse. Figure 33 shows the CV curves for the 2% Sn samples and Figure 34 shows the corresponding carrier depth profile. According to the dopant compensation hypothesis, we would expect changes in the carrier depth profiles corresponding to the changes observed in photoresponse, but this is not seen in the data. Although Figure 34 does show a large difference between the control sample and irradiated samples' depth profiles, the curves of the irradiated samples are grouped closely and do not correspond to the pattern seen in the photoresponse data. As seen in Figure 32, for the 2% Sn samples there is about a four-fold increase in photoresponse from the control sample to the high fluence sample, and about a three-fold increase between the high-fluence and low-fluence samples, so we would expect a similar jump in the depth profiles which is not seen in Figure 34.

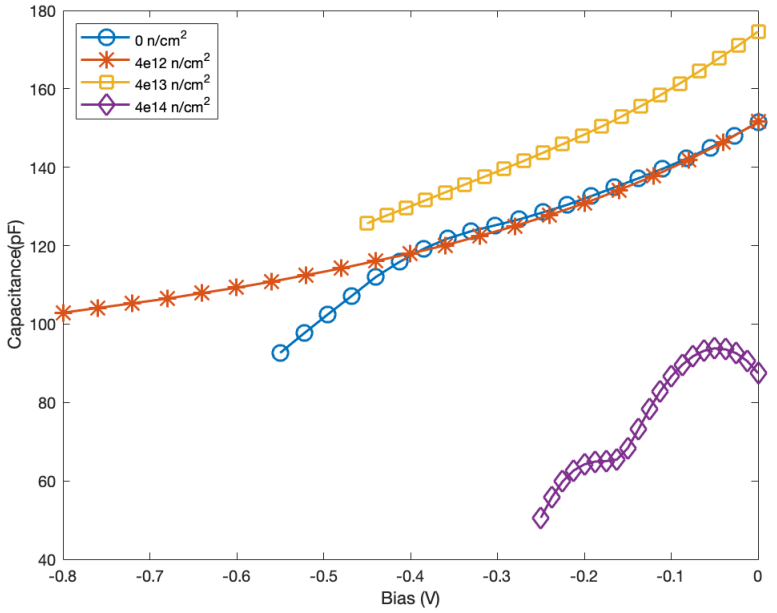

Figure 33. CV curves of 2% Sn samples. Control and low fluence samples measured at 150K, mid fluence sample measured at 175 K, and high fluence sample measured at 200 K.

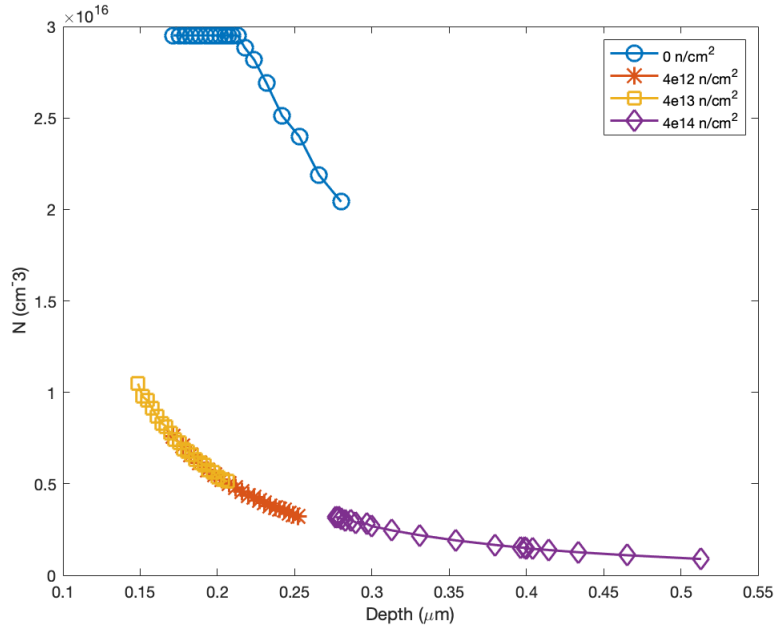

Figure 34. Carrier concentration depth profile of 2% Sn samples calculated from CV data displayed in Figure 33.

It is noteworthy that the 2% Sn samples were the only diodes that had a large difference between the depth profiles before and after irradiation. The rest of the diode types either had little change among all samples (the 5.3% Sn samples), or one outlier sample. For example, Figures 35 and 36 show a large gap in the CV and depth profile data between the low-fluence sample and the rest of the 6.8% Sn samples. In the 0% Sn samples, the high-fluence sample was the outlier, and in the 6.9% Sn samples, the mid-fluence sample was the outlier. The cause of these outliers is unknown, so the difference in CV and carrier depth profiles for the 2% Sn samples is not necessarily attributable to radiation damage.

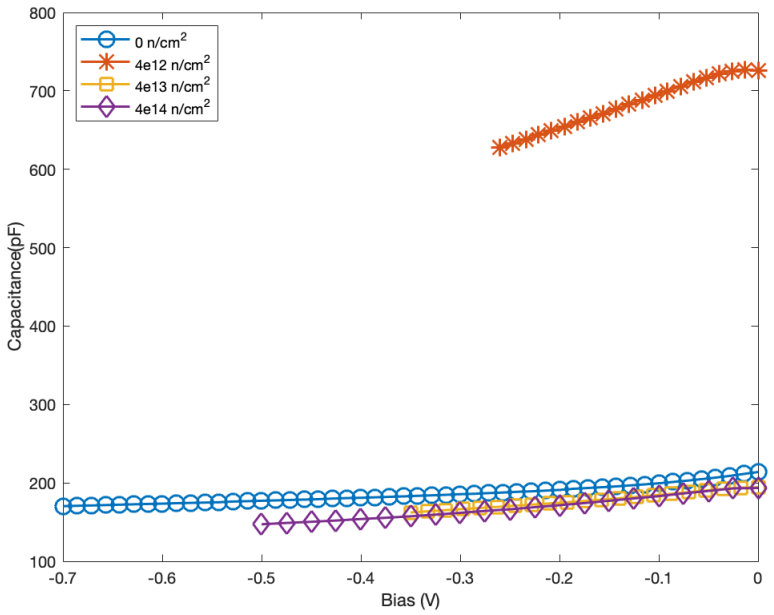

Figure 35. CV curves of 6.8% Sn samples. Mid fluence sample measured at 150 K, all other samples measured at 200 K.

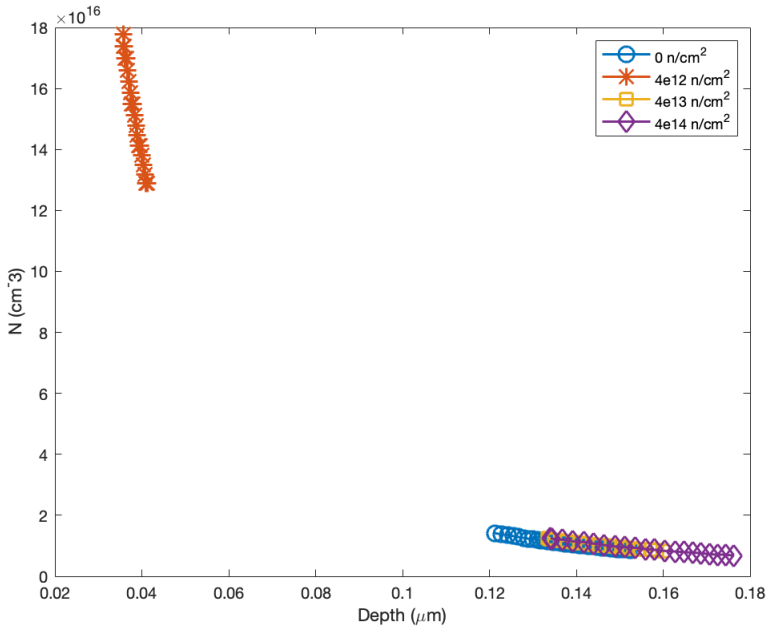

Figure 36. Carrier concentration depth profile of 6.8% Sn samples calculated from CV data displayed in Figure 35.

Although the CV curve data does not support the dopant compensation hypothesis that was considered above, it is important to note that the CV data only helps us to probe a limited area of the p-i-n. Because the carrier depth profile can only be calculated from the CV curve data in the depletion region of the p-i-n junction, the domain of each depth profile curve gives a measure of the size of the depletion region in the corresponding diode. In other words, the width of the depletion region can be estimated by subtracting the end points of the depth profile curve of each sample. As seen in Figure 34, the mid fluence sample had the smallest depletion region, approximately 60 nm, while the high fluence sample had the largest depletion region, approximately 240 nm. The depletion region was even smaller for the high tin-content samples like those shown in Figure 36 that range from approximately 5 to 40 nm. Although the depletion region is the most important part of the p-i-n diode, photodetection also happens outside of this limited region that can be

measured by CV curve measurements, so it is possible that dopant compensation is a major factor in the regions where the carrier depth profile could not be calculated. This explanation is purely speculative, so there may be other factors that cause the increase in photoresponse in these photodiodes after irradiation.

These results are similar to those found by Choe in which the majority of the diodes had little change in the carrier depth profile before and after irradiation. That study also found that the depletion region of the high tin-content samples was considerably smaller than the low tin-content samples', which matches the results found here [11] [28].

4.4 DLTFS Results

As mentioned above, good DLTFS measurements require a low leakage current and a stable CV relationship over a wide voltage range. A larger change in capacitance between the fill and measurement biases leads to better resolution. However, even the devices that were selected as having the best rectifying behavior had relatively high leakage current and an unstable CV relationship. The difference between the fill and measurement biases for most successful measurements was less than 0.3 V. This caused the resolution of the spectra to be poor, so only a few peaks were resolvable to calculate the corresponding defects' energy level. However, although the peaks were difficult to resolve, some comments can be made by analyzing the spectra.

Before presenting the results, it must be pointed out that the comparability of the spectra of different radiation fluence levels (such as the one shown in Figure 38) is limited because they could not be successfully measured with the same measurement parameters. Nevertheless, they are given to provide an idea of how increased radiation changed the spectra, most notably in the trend of converting majority carrier peaks to minority carrier peaks.

The best resolved peak was observed in the 0% sample that was irradiated with $4\times10^{14}\text{cm}^{-2}$. Figure 37 shows the spectra for different rate windows and pulse widths. The shift in the general trend gives confidence that the Fourier transform method to simulate different rate windows is trustworthy. Using the Arrhenius plot of this peak, the trap energy was determined to be at 0.26 eV below the conduction band which has been attributed previously to an A center vacancy-oxygen (V-O) defect complex [28]. This corresponds well to the major defect resolved by Choe in which a 0% Sn sample was subject to 4×10^{13} cm^{-2} of proton fluence and the trap concentration was determined to be 5×10^{15} cm^{-3}, or a defect introduction rate of 125 cm^{-1}. In the sample subject to 4×10^{14} cm^{-2} of neutron fluence, the trap concentration was determined to be 1.6×10^{14} cm^{-3}, or a defect introduction rate of 2.5 cm^{-1}. This implies that the 2 MeV protons used by Choe created about 50 times as many traps as the 1 MeV (Si) equivalent neutrons used in this study. This corresponds well to the difference in NIEL predicted by Figure 9.

Figure 38 compares the DLTFS spectra for samples at different irradiation levels. There appears to be a majority carrier trap (negative transient signal) for the zero and low fluence samples, but in the high fluence sample only minority carrier traps (positive transient signal) are observed.

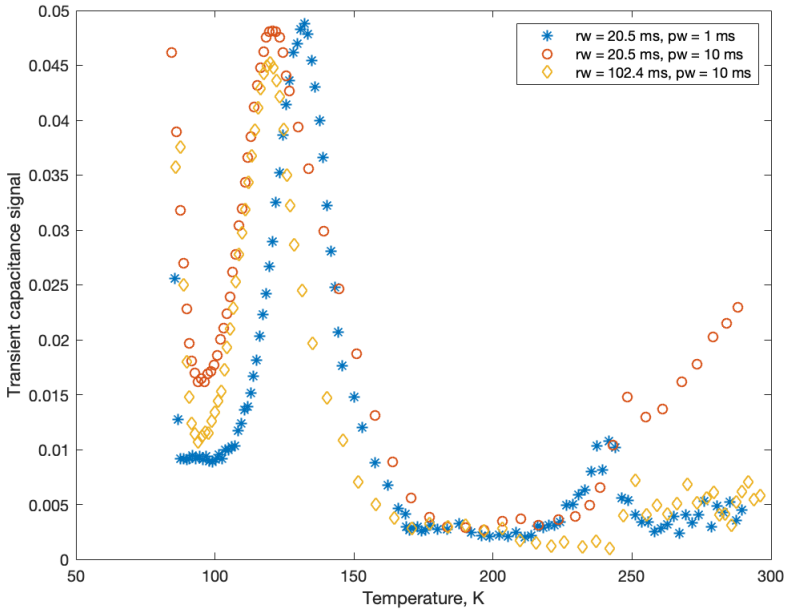

Figure 37. 0% Sn DLTFS spectra of varying rate windows (rw) and pulse widths (pw). Sample was subject to $4 \times 10^{14}\ \mathrm{cm}^{-2}$ neutron fluence. Measurement bias = -0.7 V, fill bias = 0.1 V.

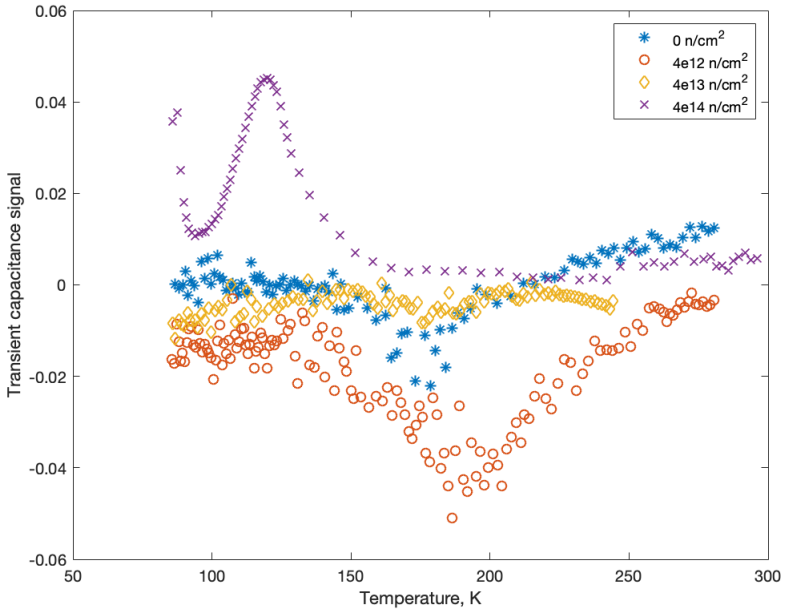

Figure 38. 0% Sn DLTFS spectra of samples subject to varying neutron fluence. Control sample: Measurement bias = -0.8 V, Fill bias = 0 V, Rate window = 205 ms, Pulse width = 10 ms. Low fluence sample: Measurement bias = -0.5 V, Fill bias = 0.15 V, Rate window = 102 ms, Pulse width = 10 ms. Mid fluence sample: Measurement bias = -0.3 V, Fill bias = 0.15 V, Rate window = 205 ms, Pulse width = 10 ms. High fluence sample: Measurement bias = -0.7 V, Fill bias = 0.1 V, Rate window = 102 ms, Pulse width = 10 ms.

As shown in Figure 39, the spectra for the 2% tin samples had much lower resolution and no peaks were successfully resolved, although there do appear to be two positive peaks near 100 K and 130 K. Figure 40 compares the samples subject to different fluence levels, but unfortunately the DLTFS spectrum of the low fluence sample could not successfully be measured. Here the strongest peaks appear to be in the mid fluence sample.

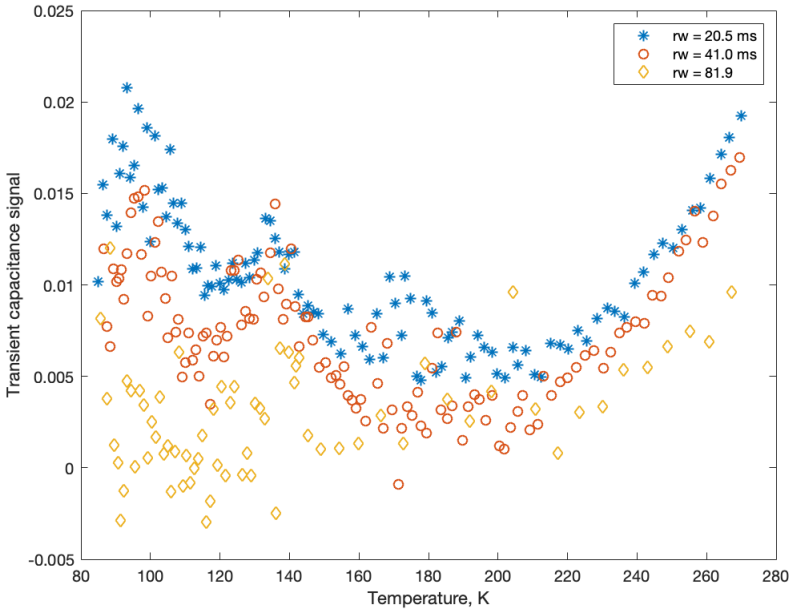

Figure 39. 2% Sn DLTFS spectra of varying rate windows (rw). Sample was subject to $4 \times 10^{13}\,\mathrm{cm}^{-2}$ neutron fluence. Measurement bias = 0.0 V, fill bias = 0.15 V, pulse width = 10 ms.

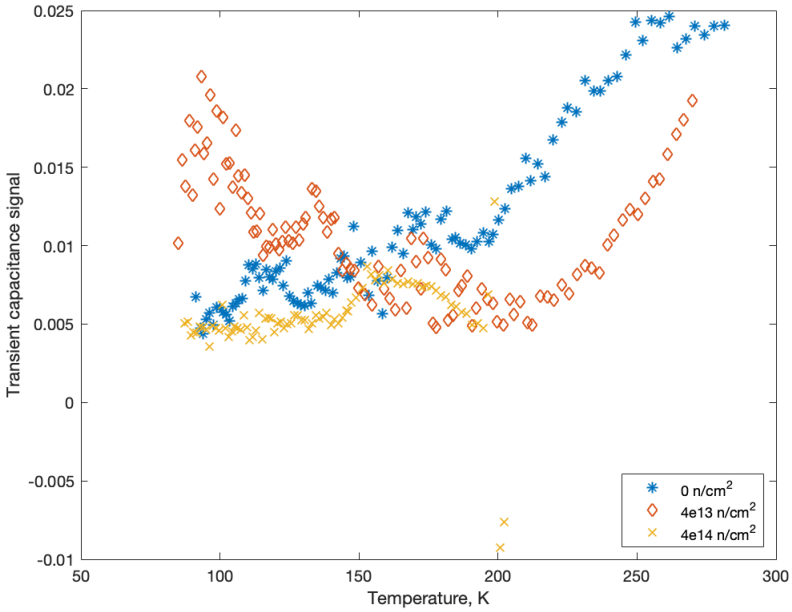

Figure 40. 2% Sn DLTFS spectra of samples subject to varying neutron fluence. Sample subject to 4×10^{12} cm^{-2} neutron fluence was unable to be measured. Control sample: Measurement bias = -0.3 V, Fill bias = 0.2 V, Rate window = 20.5 ms, Pulse width = 10 ms. Mid fluence sample: Measurement bias = 0.0 V, Fill bias = 0.15 V, Rate window = 20.5 ms, Pulse width = 10 ms. High fluence sample: Measurement bias = 0.0 V, Fill bias = 0.1 V, Rate window = 20.5 ms, Pulse width = 10 ms.

The low fluence, 5.3% Sn sample had a peak resolved as shown in Figure 41. Although the peak does not seem immediately apparent for the 20.5 ms and 102.4 ms measurements, Figure 42 shows a detail of the spectra in which the peak can be seen for all three measurements. The estimated trap energy is 0.10 eV above the valence band. This trap energy has not been attributed to a specific defect complex in previous literature. Figure 43 compares the spectra of the samples of different fluence and shows similar behavior to the 0% Sn samples in which a large majority carrier trap in the low fluence sample is replaced by a minority carrier peak in the high fluence samples.

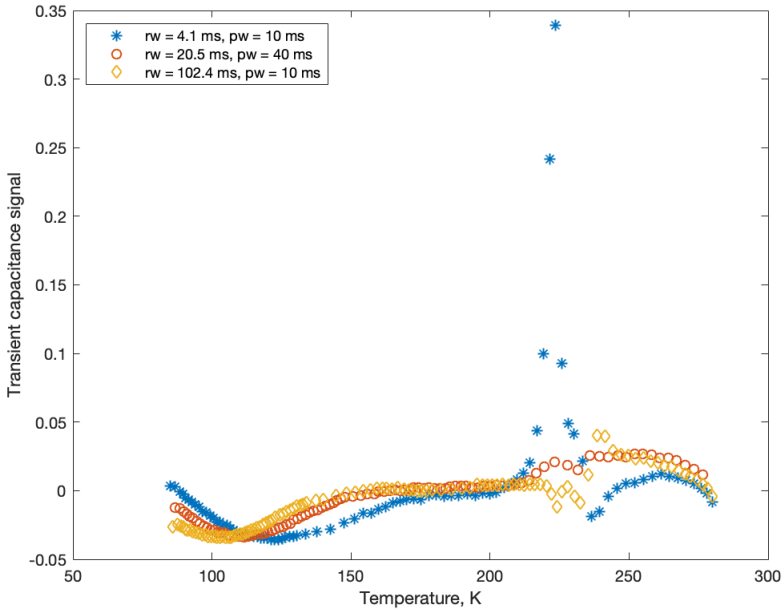

Figure 41. 5.3% Sn DLTFS spectra of varying rate windows (rw) and pulse widths (pw). Sample was subject to $4 \times 10^{12}\,\mathrm{cm}^{-2}$ neutron fluence. Measurement bias = 0.0 V, fill bias = 0.2 V.

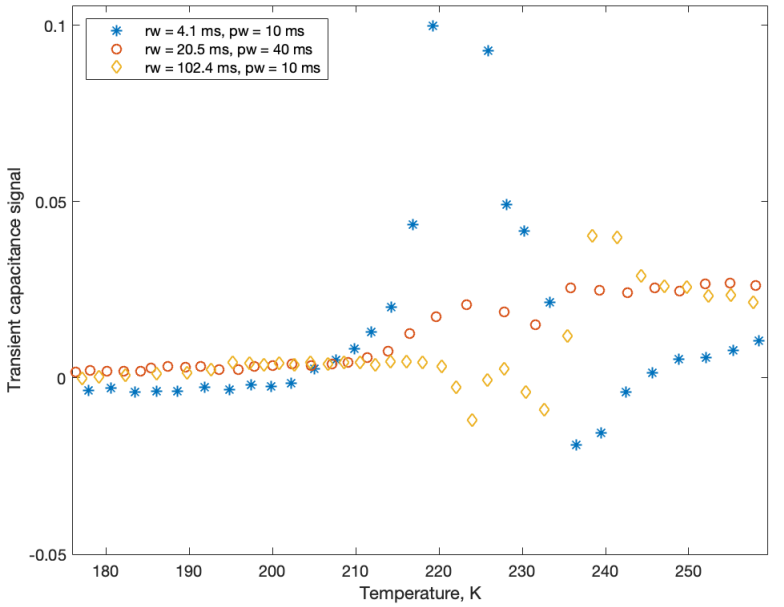

Figure 42. Detail of Figure 41

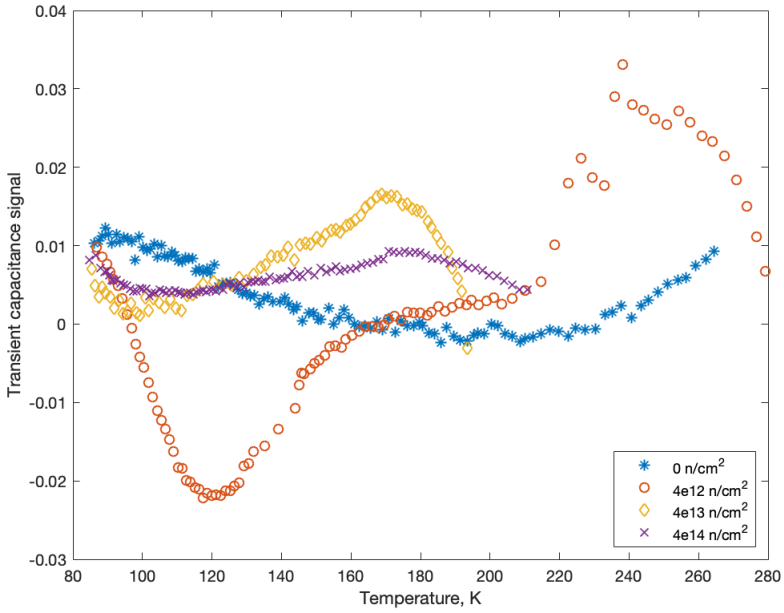

Figure 43. 5.3% Sn DLTFS spectra of samples subject to varying neutron fluence. Control sample: Measurement bias = -0.5 V, Fill bias = 0.0 V, Rate window = 20.5 ms, Pulse width = 10 ms. Low fluence sample: Measurement bias = 0.0 V, Fill bias = 0.15 V, Rate window = 20.5 ms, Pulse width = 10 ms. Mid fluence sample: Measurement bias = 0.0 V, Fill bias = 0.1 V, Rate window = 20.5 ms, Pulse width = 10 ms. High fluence sample: Measurement bias = -0.1 V, Fill bias = 0.1 V, Rate window = 20.5 ms, Pulse width = 10 ms.

Figure 44 shows the spectra for the low fluence 6.8% Sn sample. The Arrhenius plot of the peak estimates the trap energy level to be 0.17 eV which is attributed to the V-P complex. Unlike the fluence comparison for the 0% and 5.3% Sn samples in which the low fluence samples showed majority carrier peaks, Figure 45 has a majority carrier peak in the zero fluence samples while the irradiated sample spectra are dominated by minority carrier peaks.

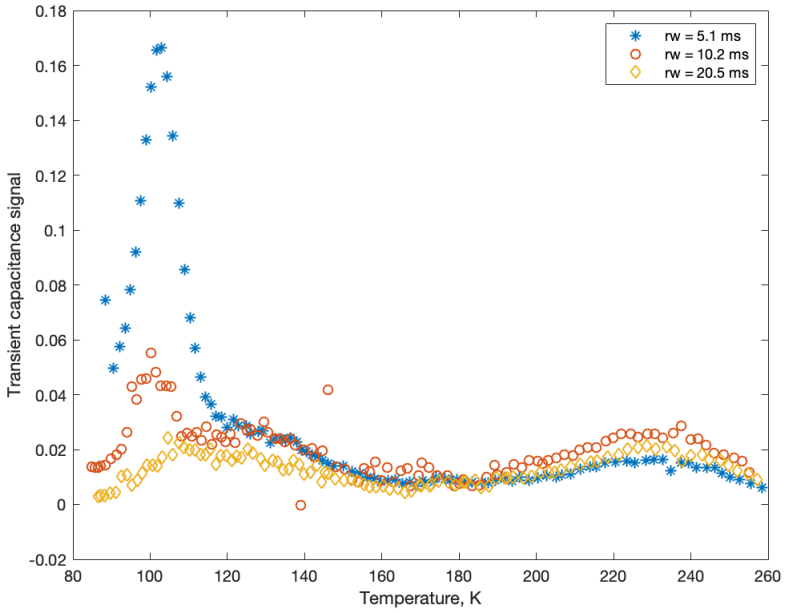

Figure 44. 6.8% Sn DLTFS spectra of varying rate windows (rw). Sample was subject to 4×10^{13} cm^{-2} neutron fluence. Measurement bias = 0.0 V, fill bias = 0.1 V, pulse width = 10 ms.

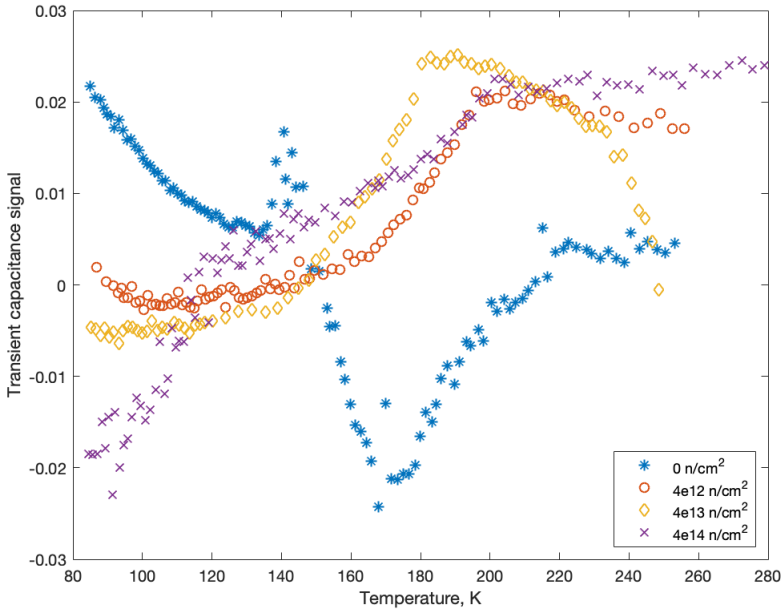

Figure 45. 6.8% Sn DLTFS spectra of samples subject to varying neutron fluence. Control sample: Measurement bias = -0.6 V, Fill bias = 0.0 V, Rate window = 20.5 ms, Pulse width = 10 ms. Low fluence sample: Measurement bias = -0.25 V, Fill bias = 0.1 V, Rate window = 10.2 ms, Pulse width = 10 ms. Mid fluence sample: Measurement bias = -0.3 V, Fill bias = 0.1 V, Rate window = 10.2 ms, Pulse width = 20 ms. High fluence sample: Measurement bias = -0.35 V, Fill bias = 0.15 V, Rate window = 10.2 ms, Pulse width = 10 ms.

Finallly, no peaks were successfully resolved for the 6.9% Sn samples, although Figure 46 does appear to have a minority carrier peak near 180 K for the low fluence sample. The mid fluence sample was not measurable, so it is not included in the comparison in Figure 47.

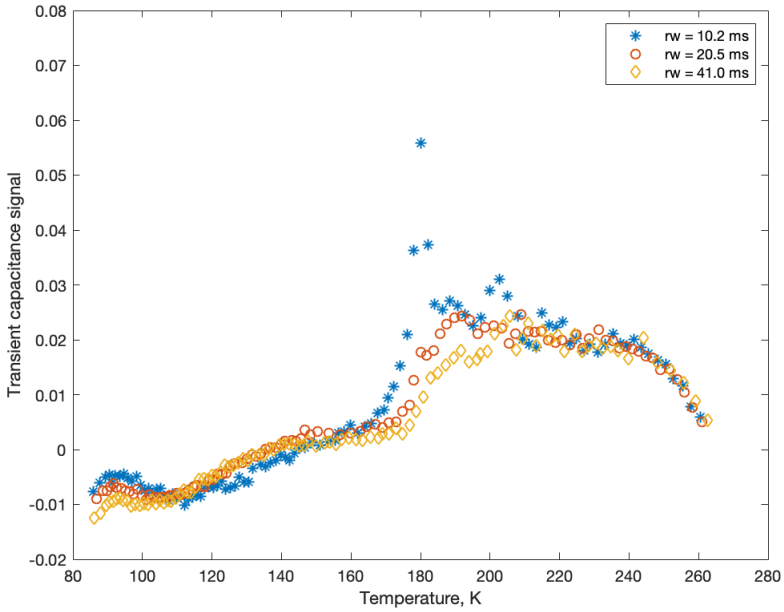

Figure 46. 6.9% Sn DLTFS spectra of varying rate windows (rw). Sample was subject to 4×10^{12} cm^{-2} neutron fluence. Measurement bias = 0.0 V, fill bias = 0.1 V, pulse width = 10 ms.

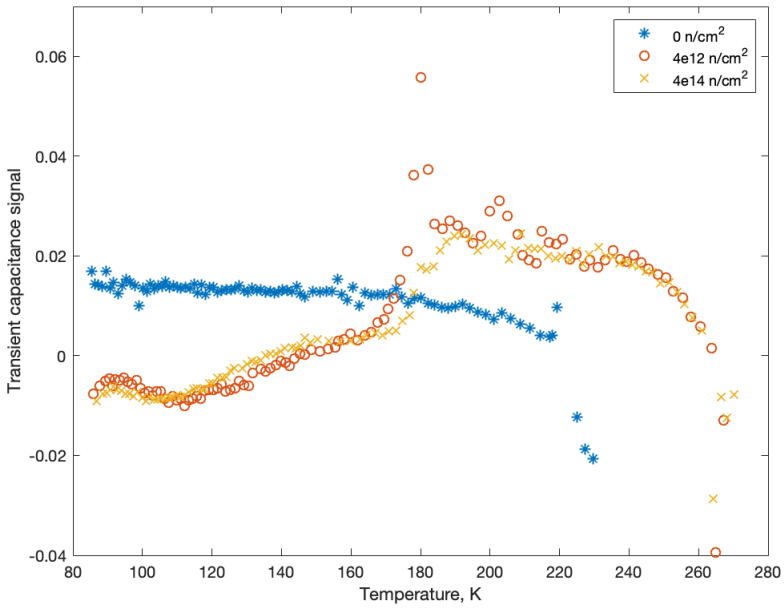

Figure 47. 6.9% Sn DLTFS spectra of samples subject to varying neutron fluence. Control sample: Measurement bias = 0.0 V, Fill bias = 0.2 V, Rate window = 20.5 ms, Pulse width = 10 ms. Low fluence sample: Measurement bias = 0.0 V, Fill bias = 0.1 V, Rate window = 10.2 ms, Pulse width = 10 ms. High fluence sample: Measurement bias = 0.0 V, Fill bias = 0.1 V, Rate window = 20.5 ms, Pulse width = 10 ms.

Although only a few defects could be identified by resolving peaks in the DLTFS spectra, the results do provide some support for the explanation given for the increase in photoresponse. With the exception of Figure 45, the spectra generally show the control samples with smaller peaks than the irradiated samples, indicating that greater neutron fluence caused greater defect concentration, as expected. Although this does not help explain the overall improvement in photoresponse observed in the irradiated samples, it does correspond with the decrease in photoresponse most of the diode types displayed going from a low to a high level of radiation fluence.

Finally, in the DLTFS spectra, especially Figures 38 and 43, electron traps generally dominate in the control samples while hole traps dominate in the irradiated samples, especially the samples subject to a high level of neutron fluence.

V. Conclusion and Future Work

5.1 Conclusions

Many of the results were contrary to expectations, but they also correspond well with past studies, particularly Choe's proton displacement damage study that used most of the same diode types as were used in this study of neutron displacement damage. Although the change in IV curves post-irradiation generally followed expectations, Choe occasionally observed changes that were contrary to expectations, such as a reduction in dark current in a 0% Sn sample after it was subject to $4 \times 10^{13}\,\mathrm{cm}^{-2}$ of proton fluence [11]. As mentioned above, it is estimated that the protons used by Choe created approximately 50 times as many traps as the neutrons used in this study, so it makes sense that his IV results would more consistently show the expected degradation in rectifying behavior of the diodes.

Although the unexpected increase in post-irradiation photoresponse is not completely unprecedented in radiation damage studies of photodiodes [22], the magnitude of the increase is much greater than anything found in the literature. The mechanism that caused this increase is unknown. Dopant compensation was presented as a hypothesis, but it is not supported by the CV curve and carrier depth profile data which (similar to Choe's results) showed little variation before and after irradiation. It is recognized that the depth profiles only give information about the depletion region of the p-i-n junction and that, although the depletion region is the most important region for absorbing light, photodetection is not exclusive to this region. This means we have no data to characterize the diode in a large part of the p-i-n junction, particularly in the high tin-content samples in which the depletion region is considerably smaller than in the low tin-content samples.

Although the DLTS spectra were not as clear as in Choe's study and only three

peaks were resolved in all of the samples, the general trends of the DLTS results corresponded well with expectations. Generally, electron traps dominated in the control samples while hole traps dominated in the irradiated samples, especially the samples subject to a high level of neutron fluence. One peak in the 0% Sn sample was resolved that matched a trap resolved by Choe and estimated to have a trap energy level at 0.26 eV below the conduction band [11]. Comparison of the concentrations of these two peaks yielded the aforementioned determination that the 2 MeV protons used by Choe created approximately 50 times as many traps as the 1 MeV (Si) equivalent neutrons used in this study.

Finally, the results support Choe's conclusion that increasing the tin content of the GeSn alloy used in the photodiode has the benefit of making the device more resistant to radiation damage and the drawback of degrading the rectifying behavior of the device. These are important considerations that will influence the use of this material in future potential applications as a room-temperature near-to-mid infrared detector.

5.2 Future Work

Due to the unexpected nature of the results, it would be desirable to repeat experiments, particularly if GeSn diode samples could be obtained from a source different from the one used in this study. This would help indicate if the observed trait of improved photoresponse is limited only to diodes produced at ASU and therefore attributable to the fabrication process. If however GeSn samples from a different producer duplicated the improved photoresponse, it would support the idea that this behavior is characteristic of the physical properties of GeSn diodes and would warrant further study. The responsivity measurements should also be repeated at varying bias levels to observe if the magnitude of the improvement is exaggerated for

zero bias measurements.

Because of the large leakage current and unstable CV relationship in the samples, it was difficult to predict the optimal DLTFS settings, so some trial and error was necessary to produce the spectra reported in this study. This made spectrum comparison especially problematic because early measurements were made with settings that were unable to produce good results for later measurements. More DLTFS measurements would be helpful to ascertain that the optimal settings are found, and attempt to mitigate the differences in settings to facilitate spectrum comparison. The relatively low trap production due to the neutrons also made it difficult to detect and resolve peaks in the DLTFS spectra, so the experiment could be repeated at a higher neutron flux which should make DLTFS analysis less challenging.

To estimate the defect concentrations of the resolved peaks, those spectra need to be repeated with increasing pulse widths. Because a short pulse width does not completely fill the trap, increasing the pulse width can increase the size of the peak observed on the DLTFS spectrum. When the peak does not grow any more with an increased pulse width, the trap has been completely filled and the trap concentration can be properly estimated. These measurements would facilitate spectrum comparison between samples used in this study and with other DLTS measurements made for similar investigations.

There are several defect characterization methods aside from DLTS that could be beneficial to understand how displacement damage affects GeSn photodiodes. The thermally stimulated current (TSC) technique is another electrical characterization technique that is often used when DLTS measurements are not satisfactory [51]. Positron annihilation spectroscopy could be used to study the void size of defects, but it requires preparation of samples less than 0.5 mm thick [52]. Electron paramagnectic resonance spectroscopy could be used to determine the atomic structure of point

defects. Finally, high resolution transmission electron spectroscopy could be used to determine the defect density in any cluster formation, but sample preparation is quite challenging [51]. Given the relative challenges and cost of these techniques, it seems advisable to continue defect characterization with a TSC study.

Appendix: Photodiode p-i-n Schematics

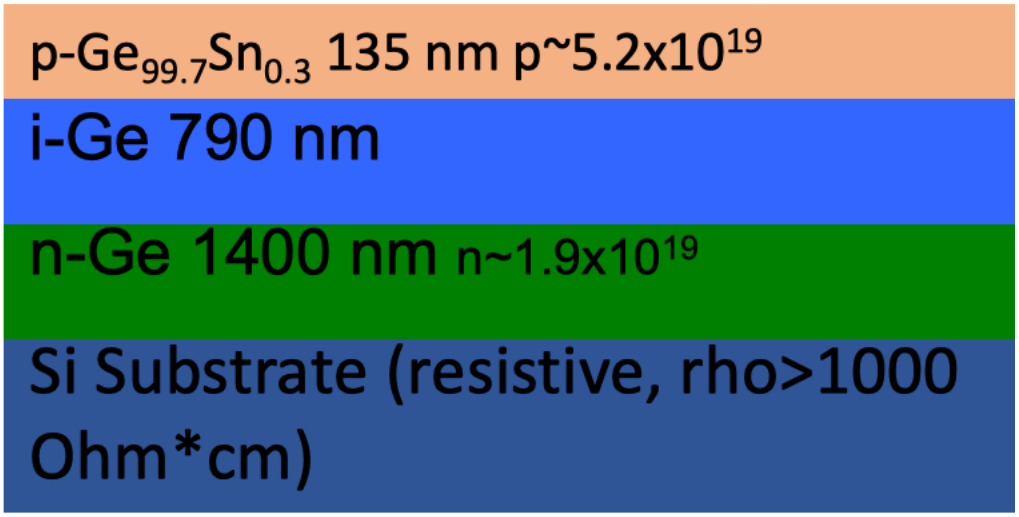

Figure 48. Ge472 schematic.

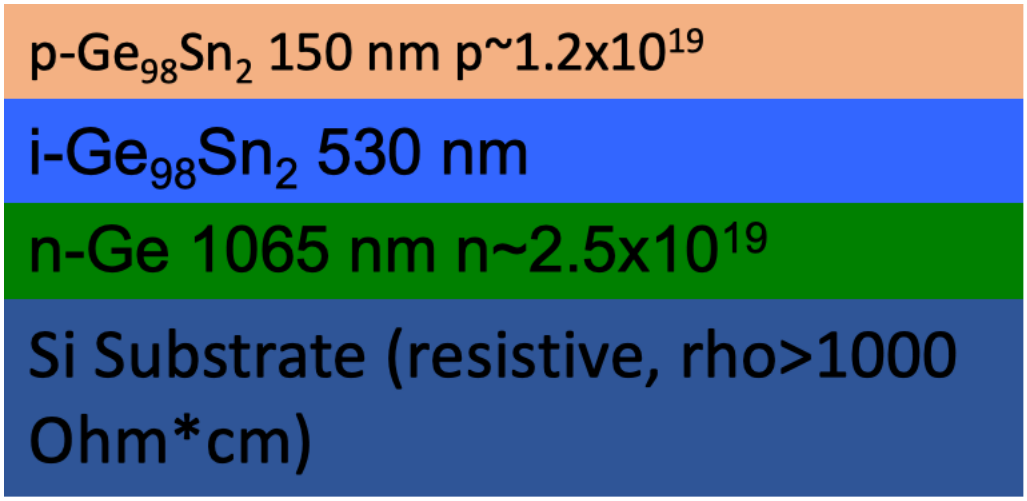

Figure 49. GeSnGePiN13 schematic.

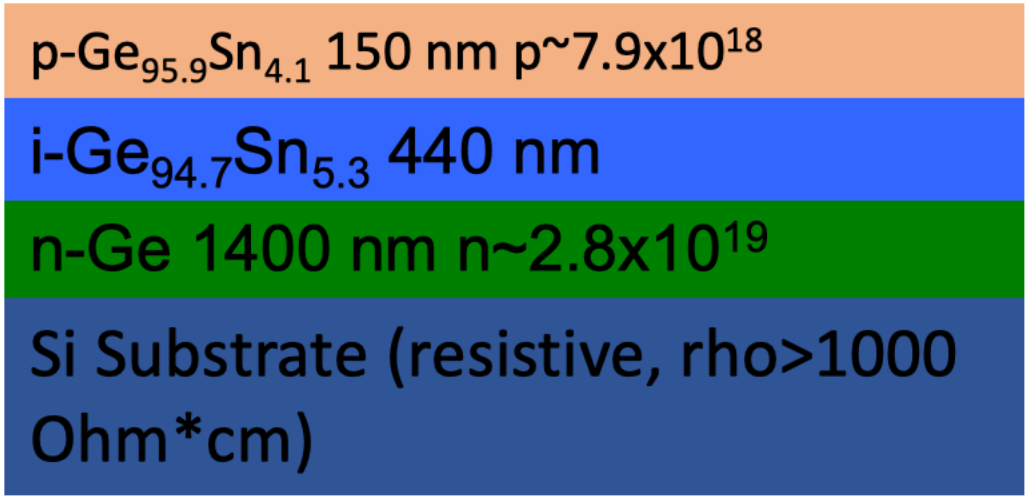

Figure 50. GeSnGePiN9A schematic.

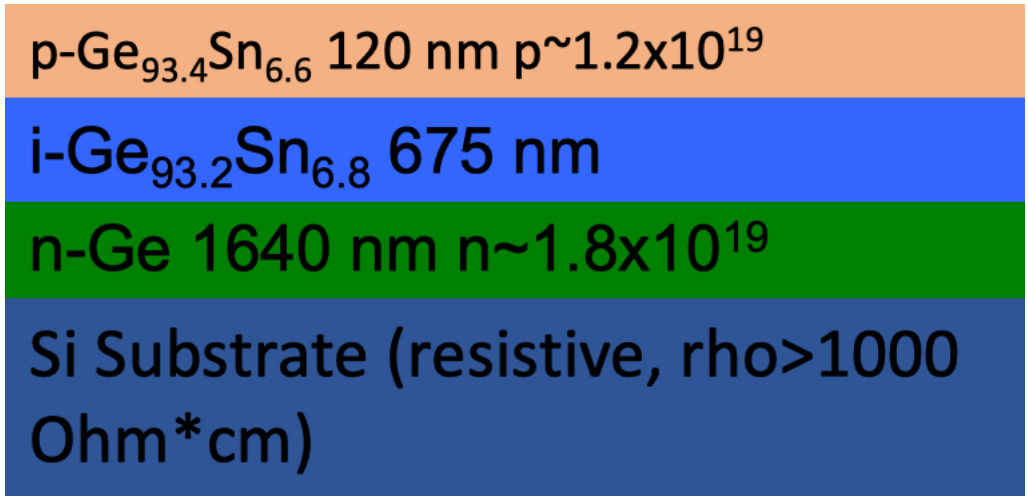

Figure 51. GeSnGePiN60A schematic.

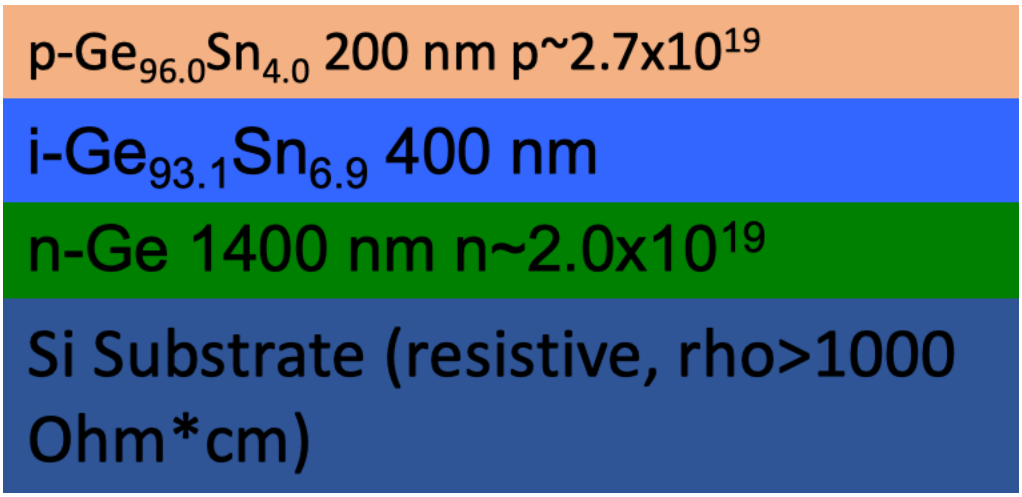

Figure 52. GeSnGePiN12 schematic.

Bibliography

1. A. K. Sood, J. W. Zeller, Y. R. Puri, C. Rouse, P. Haldar, H. Efstathiadis, N. K. Dhar, and P. S. Wijewarnasuriya, "SiGe focal plane array detector technology for near-infrared imaging," *International Journal of Engineering Research and Technology*, vol. 10, no. 1, pp. 81–103, 2017.

2. M. McPherson, B. Jones, and T. Sloan, "Effects of radiation damage in silicon p-i-n photodiodes," *Semiconductor Science and Technology*, vol. 12, pp. 1187–1194, July 1997.

3. J. Kim, "Band structure calculations of strained semiconductors using empirical pseudopotential theory," Doctoral Dissertation, University of Massachusetts Amherst, February 2011.

4. R. Geiger, T. Zabel, and H. Sigg, "Group IV direct band gap photonics: methods, challenges, and opportunities," *Frontiers in Materials and Frontiers in Physics*, vol. 2, pp. 81–98, July 2015.

5. C. J. Marshall and P. W. Marshall, *Proton Effects and Test Issues for Satellite Designers: Displacement Effects*. Nuclear Space and Radiation Effects Conference, 1999.

6. G. D. Watkins and J. W. Corbett, "Defect in irradiated silicon. I. electron spin resonance of the Si-A center," *Physical Review*, vol. 121, pp. 1001–1014, February 1960.

7. E. C. Auden, "Heavy-ion induced single particle displacement damage in silicon," Doctoral Dissertation, Vanderbilt University, December 2013.

8. P. W. Marshall, C. J. Dale, G. P. Summers, E. A. Wolicki, and E. A. Burke, "Proton, neutron and electron-induced displacement damage in germanium," *IEEE Transactions on Nuclear Science*, vol. 36, pp. 1882–1888, Dec 1989.

9. S. Hamady, "A simulation of doping and trap effects on the spectral response of *AlGaN* ultraviolet detectors," *Journal of Semiconductors*, vol. 33, Mar 2012.

10. D. Lang, "Deep-level transient spectroscopy: A new method to characterize traps in semiconductors," *Journal of Applied Physics*, vol. 45, pp. 3023–3032, July 1974.

11. K. Choe, "Displacement damage effects in GeSn light emitting diodes," Master's Thesis, Air Force Institute of Technology, March 2019.

12. C. Callan, J. Goodman, M. Cornwall, N. Fortson, R. Henderson, J. Katz, D. Long, R. Muller, M. Ruderman, and J. Vesecky, "Sensors to support the soldier," *JSR-04-210*, 2005.

13. R. Reed and S. Buchner, *Guideline for Ground Radiation Testing and Using Optocouplers in the Space Radiation Environment*. NASA/Goddard Space Flight Center, 2002.

14. N. S. Andreas, "Space-Based Infrared System (SBIRS) system of systems," *IEEE Aerospace Conference*, vol. 4, 1997.

15. K. W. Ang and G. Q. Lo Patrick, "Avalanche photodiodes: Si charge avalanche enhances APD sensitivity beyond 100 GHz," *Laser Focus World*, vol. 46, no. 8, 2010.

16. E. Kasper, M. Kittler, M. Oehme, and T. Arguirov, "Germanium tin: silicon photonics toward the mid-infrared," *Photonics Research*, vol. 1, pp. 69–76, Aug 2013.

17. J. D. Gallagher, "The optical and electronic properties of $Ge_{1-y}Sn_y$ and $Ge_{1-x-y}Si_xSn_y$ materials and devices for silicon-integrated optoelectronics," Doctoral Dissertation, Arizona State University, December 2015.

18. K. Wittenburg, "Radiation damage in pin-photodiodes," *Nuclear Instruments and Methods in Physics Research*, vol. 270, pp. 56–61, November 1988.

19. J. Gallagher, C. Senaratne, P. Sims, T. Aoki, J. Menendez, and J. Kouvetakis, "Electroluminescence from GeSn heterostructure pin diodes at the indirect to direct transition," *Applied Physics Letters*, vol. 106, Mar 2015.

20. J. Troska, K. Gill, R. Grabit, and F. Vasey, *Neutron, proton, and gamma radiation effects in candidate InGaAs p-i-n photodiodes for the CMS tracker optical links*. CERN, 1997.

21. K. A. Gill, C. Aguilar, C. Azvedo, V. P. Arbet-Engels, J. Batten, G. Cervelli, R. Grabit, F. B. H. Jensen, C. Mommaert, J. Troska, and F. Vasey, "Radiation damage studies of optical link components for applications in future high-energy physics experiments," in *Photonics for Space Environments VI* (E. W. Taylor, ed.), vol. 3440, pp. 89 – 99, International Society for Optics and Photonics, SPIE, 1998.

22. E. Blansett, D. K. Serkland, M. J. Cich, K. M. Geib, G. M. Peake, R. M. Fleming, D. L. Wrobel, and T. F. Wrobel, *Final Report on LDRD Project 105967: Exploring the Increase in GaAs Photodiode Responsivity with Increased Neutron Fluence*. Sandia National Laboratories, 2008.

23. C. G. Carlone, G. Bernier, E. Tannous, S. Khanna, W. Anderson, and J. W. Gerdes, "The photoluminescent spectrum of neutron irradiated GaAs," *IEEE Transactions on Nuclear Science*, vol. 37, pp. 1718–1725, December 1990.

24. E. M. Gullikson, R. Korde, L. R. Canfield, and R. E. Vest, "Stable silicon photodiodes for absolute intensity measurements in the VUV and soft x-ray regions," *Journal of Electron Spectroscopy and Related Phenomena*, vol. 80, pp. 313–316, 1996.

25. E. Blansett, D. K. Serkland, M. J. Cich, K. M. Geib, G. M. Peake, R. M. Fleming, D. L. Wrobel, and T. F. Wrobel, *Final Report on LDRD Project 52722 Radiation Hardened Optoelectronics Components for Space-Based Applications*. Sandia National Laboratories, 2003.

26. S. M. Khanna, C. Rejeb, A. Jorio, M. Parenteau, C. Carlone, and J. W. J. Gerdes, "Electron and neutron radiation-induced order effect in gallium arsenide," *IEEE Transactions on Nuclear Science*, vol. 40, pp. 1350–1359, December 1993.

27. K. Choe, M. Hogsed, N. Miguel, and J. McClory, "Displacement damage effects in germanium tin light emitting diodes," *Journal of Radiation Effects, Research, and Engineering (submitted)*, 2019.

28. M. Hogsed, K. Choe, N. Miguel, B. Wang, and J. Kouvetakis, "Radiation-induced electron and hole traps in $Ge_{1-x}Sn_x$," *Journal of Applied Physics (submitted)*, 2019.

29. M. C. Petersen, A. N. Larsen, and A. Mesli, "Divacancy defects in germanium studied using deep-level transient spectroscopy," *Physical Review B*, vol. 82, 2010.

30. V. P. Markevich, A. R. Peaker, B. Hamilton, V. V. Litvinov, Y. M. Pokotilo, S. B. Lastovskii, J. Coutinho, A. Carvalho, M. J. Rayson, and P. R. Briddon, "Tin-vacancy complex in germanium," *Journal of Applied Physics*, vol. 109, March 2011.

31. M. Mamor, M. Elzain, K. Bouziane, and S. Al Harthi, "Deep-level transient spectroscopy study of the E center in n-Si and partially relaxed in n-$Si_{0.9}Ge_{0.1}$ alloy layers,"

32. V. P. Markevich, I. D. Hawkins, A. R. Peaker, K. V. Emtsev, E. V. V., V. V. Litvinov, L. I. Murin, and L. Dobaczewski, "Vacancy-group-V-impurity atom pairs in Ge crystals doped with P, As, Sb, and Bi," *Physical Review B*, vol. 70, 2004.

33. R. F. Pierret, *Semiconductor Device Fundamentals*. No. 2, Pearson Education Inc. and Dorling Kindersley Publishing Inc., 1996.

34. N. Palit, U. Dutta, and P. Chatterjee, "Detailed computer modeling of semiconductor devices," *Indian Journal of Physics*, vol. 80, no. 1, pp. 11–35, 2006.

35. P. Y. Yu and M. Cardona, *Fundamentals of Semiconductors: Physical and Material Properties*. No. 3, Springer, 2005.

36. L. Jiang, J. D. Gallagher, C. L. Senaratne, T. Aoki, J. Mathews, J. Kouvetakis, and J. Menéndez, "Compositional dependence of the direct and indirect band gaps in $Ge1-ySn_y$ alloys from room temperature photoluminescence: implications for the indirect to direct gap crossover in intrinsic and n-type materials," *Semiconductor Science and Technology*, vol. 29, p. 115028, oct 2014.

37. V. P. Markevich, I. P. A. Hawkins, V. V. Litvinov, L. Dobaczewski, and J. Lindstrom, "Electronic properties of vacancy-oxygen complex in ge crystals,"

38. S. Zaima, N. Osamu, N. Taoka, M. Kurosawa, W. Takeuchi, and M. Sakashita, "Growth and applications of GeSn-related group-IV semiconductor materials," *Science and Technology of Advanced Materials*, vol. 1, pp. 69–76, Aug 2015.

39. D. K. Schroeder, *Semiconductor Material and Device Characterization*. No. 2, Wiley-Interscience, 1998.

40. J. R. Srour and R. A. Hartmann, "Enhanced displacement damage effectiveness in irradiated silicon devices," *IEEE Transactions on Nuclear Sciences*, vol. 36, pp. 1825–1830, December 1989.

41. A. Homes-Siedle and L. Adams, *Handbook of Radiation Effects*. No. 2, Oxford University Press, 2002.

42. K. W. Busch and M. A. Busch, *Multielement Detection Systems for Spectrochemical Analysis*. Wiley-Interscience, 1990.

43. A. Friedman, *An Augmented drift-diffusion formulation in semiconductor devices. In: Mathematics in Industrial Problems. The IMA Volumes in Mathematics and its Applications.* No. 38, Springer, 1991.

44. F. C. Treble, "The effects of radiation damage in solar cells," *Microelectronics Reliability*, vol. 1, pp. 299–300, March 1962.

45. A. S. Tremsin and O. H. W. Siegmund, "Stability of quantum efficiency and visible light rejection of alkali halide photocathodes," in *UV, Optical, and IR Space Telescopes and Instruments* (J. B. Breckinridge and P. Jakobsen, eds.), vol. 4013, pp. 411 – 420, International Society for Optics and Photonics, SPIE, 2000.

46. A. Turut, A. Karabulut, K. Ejderha, and N. Bıyıklı, "Capacitance–conductance characteristics of $Au/Ti/Al_2O_3$ n -GaAs structures with very thin Al_2O_3 interfacial layer," *Materials Research Express*, vol. 2, p. 046301, 04 2015.

47. D. Johnstone, *Deep Level Transient Spectroscopy: System User's Manual*. Semetrol, LLC, 2014.

48. S. Weiss and R. Kassing, "Deep level transient fourier spectroscopy: A technique for the analysis of deep level properties," *Solid-State Electronics*, vol. 31, pp. 1733–1742, June 1988.

49. "NRL irradiation facility neutron fluxes and neutron gamma dose rates." Online, 2019.

50. S. R. Systems, "About lock-in amplifiers." Online, 2011.

51. I. Pintilie, L. Nistor, S. Nistor, and A. Joita, "Experimental techniques for defect characterization of highly irradiated materials and structures," p. 033, 02 2017.

52. F. Tuomisto and I. Makkonen, "Defect identification in semiconductors with positron annihilation: Experiment and theory," *Review of Modern Physics*, vol. 85, p. 1583, 11 2013.

REPORT DOCUMENTATION PAGE

Form Approved
OMB No. 0704–0188

1. REPORT DATE *(DD–MM–YYYY)*	2. REPORT TYPE	3. DATES COVERED *(From — To)*
26–03–2020	Master's Thesis	June 2018 — March 2020

4. TITLE AND SUBTITLE

Neutron Displacement Damage in Germanium Tin Photodiodes

5a. CONTRACT NUMBER

5b. GRANT NUMBER

5c. PROGRAM ELEMENT NUMBER

6. AUTHOR(S)

Gale, Nathan J., Second Lieutenant, USAF

5d. PROJECT NUMBER

20ENP

5e. TASK NUMBER

5f. WORK UNIT NUMBER

7. PERFORMING ORGANIZATION NAME(S) AND ADDRESS(ES)

Air Force Institute of Technology
Graduate School of Engineering and Management (AFIT/ENP)
2950 Hobson Way
WPAFB OH 45433-7765

8. PERFORMING ORGANIZATION REPORT NUMBER

AFIT-ENP-MS-20-M-096

9. SPONSORING / MONITORING AGENCY NAME(S) AND ADDRESS(ES)

Air Force Office of Scientific Research
AFOSR/RTA
8725 North Randolph Street
Arlington, Virginia 22203-1768

10. SPONSOR/MONITOR'S ACRONYM(S)

AFOSR/RTA

11. SPONSOR/MONITOR'S REPORT NUMBER(S)

12. DISTRIBUTION / AVAILABILITY STATEMENT

DISTRIBUTION STATEMENT A:
APPROVED FOR PUBLIC RELEASE; DISTRIBUTION UNLIMITED.

13. SUPPLEMENTARY NOTES

14. ABSTRACT

GeSn is a promising material for photodiodes in the near-to-mid infrared (IR) spectrum because of new growth methods that enable integration with complementary metal oxide semiconductor (CMOS) technology. While natural germanium has a threshold wavelength of 1800 nm, 6.9% Sn content extends the threshold wavelength to 2700 nm based on a Sn content dependent bandgap. Also, unlike other semiconductors that require liquid nitrogen cooling to act as an IR sensor, GeSn can be operated at room temperature, enabling a wide variety of applications. In this study, photodiodes ranging from 0% to 6.9% tin content were subjected to 1 MeV (Si) equivalent neutron radiation ranging from 4×10^{12} cm^{-2} to 4×10^{14} cm^{-2}. IV curves, CV curves, and relative photoresponse were measured before and after irradiation to observe change due to displacement damage. While the change in IV measurements varied widely, the photoresponse more than doubled for all irradiated samples, contrary to expectation. The samples of low tin content had a greater increase (as much as 1100%) than high tin content samples (ranging from 100% to 400%). Deep-level transient Fourier spectroscopy (DLTFS) was also used to measure defect levels. The 0% and 6.8% tin samples showed defects at energies of 0.26 eV below the conduction band and 0.17 eV above the valence band, respectively. The 0.26 eV trap is attributed to an A center vacancy-oxygen (V-O) complex and the 0.17 eV trap is attributed to a vacancy-phosphorous (V-P) defect.

15. SUBJECT TERMS

radiation effects, germanium tin, photodiodes, deep level transient spectroscopy

16. SECURITY CLASSIFICATION OF:			17. LIMITATION OF ABSTRACT	18. NUMBER OF PAGES	19a. NAME OF RESPONSIBLE PERSON
a. REPORT	b. ABSTRACT	c. THIS PAGE			Dr. John McClory, AFIT/ENP
U	U	U	U	89	19b. TELEPHONE NUMBER *(include area code)* (937) 255-3636, x7308; john.mcclory@afit.edu